Slew Maneuver Constraints for Agile Flexible Spacecraft

Michael A. Marshall* and Sergio Pellegrino†
California Institute of Technology, Pasadena, California, 91125

Traditional spacecraft design paradigms rely on stiff bus structures with comparatively flexible appendages. More recent trends, however, trade deployed stiffness for packaging efficiency to stow apertures with larger areas inside existing launch vehicles. By leveraging recent advances in materials and structures, these spacecraft may be up to several orders of magnitude lighter and more flexible than the current state-of-the-art. Motivated by the goal of achieving agility despite structural flexibility, this paper proposes a quantitative method for determining structure-based performance limits for maneuvering flexible spacecraft. It then uses a geometrically nonlinear flexible multibody dynamics model of a representative very flexible spacecraft to verify this method. The results demonstrate that, contrary to common assumptions, other constraints impose more restrictive limits on maneuverability than the dynamics of the structure. In particular, it is shown that the available attitude control system momentum and torque are often significantly more limiting than the compliance of the structure. Consequently, these results suggest that there is an opportunity to design less-conservative, higher-performance space systems that can either be maneuvered faster, assuming suitable actuators are available, or built using lighter-weight, less-stiff architectures that move the structure-based performance limits closer to those of the rest of the system.

I. Introduction

A current paradigm in spacecraft design trades deployed structural stiffness against packaging efficiency to build higher-performing spacecraft with larger deployed apertures that can be stowed within existing launch vehicles. Such spacecraft are currently envisioned for a variety of applications including astronomy [1]; planetary [2] and solar system exploration [3]; space science [4]; communications, power transfer, and remote sensing [5]; and space solar power [6]. Each application requires attitude slew maneuvers, i.e., maneuvers that change the spacecraft's orientation. Large-angle slew maneuvers in particular are commonly used, e.g., for reorienting sensors, antennas, and solar arrays. Slew maneuvers are an overhead on a mission, meaning they are required for achieving the mission objectives, but generally represent time lost from actively performing useful mission functions. For this reason, minimizing slew times has important implications for space mission design. In particular, slewing faster leaves more time available for executing a spacecraft's intended mission.

Given the proliferation of applications for flexible spacecraft, a common question during mission concept development and preliminary design pertains to how fast these spacecraft can be slewed. In some cases, a rapid slew capability can even be a prerequisite for feasibility and/or viability of a particular mission concept. For example, in geostationary Earth orbit (GEO), the space solar power satellites proposed by the Caltech Space Solar Power Project (SSPP) [6] require two 90-deg pitch-axis slews per day to maximize the energy delivered to the electrical grid [7]. In the SSPP concept, the system efficiency decreases as the slew time increases [8]. All else being equal, slower slew maneuvers result in the transmission of less energy, thereby increasing the cost of the electricity delivered to the grid. Thus, the slew time directly impacts the system's overall economic viability. More generally, as the development of increasingly large and flexible spacecraft continues, so too does the importance of slew time as a design driver.

A common assumption about flexible spacecraft is that structural compliance limits how fast they can be slewed. For highly compliant structures, very long slew times can make an otherwise promising mission concept infeasible. As a result, it is important to demonstrate the feasibility of slewing large flexible spacecraft early in the design process. However, to the authors' knowledge, there is no standard framework for rigorously quantifying how fast flexible spacecraft can be slewed. The most common heuristic states that the minimum slew time must be at least ten times the

*Graduate Research Assistant, Graduate Aerospace Laboratories, 1200 E. California Blvd., Mail Code 105-50. Member AIAA. Currently: Guidance and Control Analyst, The Johns Hopkins University Applied Physics Laboratory, 11100 Johns Hopkins Road, Laurel, Maryland 20723. michael.a.marshall@jhuapl.edu.

†Joyce and Kent Kresa Professor of Aerospace and Civil Engineering, Graduate Aerospace Laboratories, 1200 E. California Blvd., Mail Code 105-50. AIAA Fellow. sergiop@caltech.edu.

structure's lowest natural period. Such a heuristic is convenient but may lead to overly conservative, and in some cases, prohibitively conservative spacecraft designs and mission scenarios.

Motivated by the goal of achieving agility despite structural flexibility, this paper proposes a framework for using reduced-order models to predict minimum slew times for flexible spacecraft. The reduced-order models lead to simple analytical and quasi-analytical slew time estimates, which in turn are useful for both requirements definition and for establishing the feasibility of slewing flexible spacecraft during concept development and preliminary design.

Slew time verification then requires higher-fidelity analysis tools, such as geometrically nonlinear finite element simulations. There are many academic examples in the literature that apply these types of simulations to flexible spacecraft with simple structural geometries consisting of beams or plates; see e.g., [9, 10]. These types of simulations are also often used for modeling solar sails [11, 12] and other advanced concepts [13]. However, they are by no means standard for simulating the attitude dynamics of flexible spacecraft with complex structural geometries. To that end, this paper uses geometrically nonlinear finite element simulations of a very flexible spacecraft with a complex structural geometry both to verify slew time predictions and to promote the more widespread adoption of these types of simulations in spacecraft engineering practice.

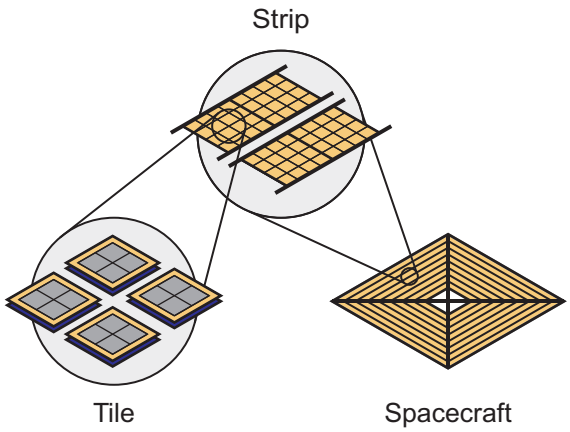

Fig. 1 Caltech SSPP spacecraft structural architecture originally introduced in [6].

As a case study, this paper analyzes a representative problem based on the Caltech SSPP spacecraft structural architecture [6] (see Fig. 1) during a 90-deg, nominally rest-to-rest pitch-axis slew maneuver. Such a maneuver is representative of the maneuvers required to maximize the energy delivered to an electrical grid from an SSPP spacecraft in GEO [7]. In the SSPP concept, the structural architecture is planar to facilitate packaging and deployment using a kirigami-inspired folding scheme and is designed to be both modular and scalable, allowing the same basic components (the photovoltaic-powered radio-frequency tiles and the structural strips) to be used for spacecraft designed for different applications at different length scales. This paper specifically considers spacecraft with outermost strips that range from 5 m to 50 m long, corresponding to first-mode natural frequencies between approximately 1 Hz and 1 mHz. The SSPP architecture and its derivatives (see e.g., [14]) are representative of a class of spacecraft structures referred to as bending architectures [15], i.e., structural concepts that derive their load carrying capability from the bending stiffness of the structural elements. With its approximately 100 g/m^2 areal density, the SSPP concept specifically occupies a middle ground in terms of stiffness and areal density between membrane-based deployable structures concepts like solar sails and more traditional spacecraft with deployable solar arrays and antennas.

This paper is organized as follows: Sec. II describes the canonical model for flexible spacecraft attitude dynamics. Sec. III uses the Craig-Bampton method [16] to develop reduced-order modal models from flexible spacecraft finite element models that are analogous to this canonical model. Sec. IV proposes a framework for predicting slew times for flexible spacecraft. Sec. V applies the tools from Secs. III and IV to predict the minimum slew times for a flexible spacecraft based on the Caltech SSPP spacecraft structural architecture. It subsequently verifies these predictions using geometrically nonlinear simulations of a high-fidelity finite element model. The paper concludes with a discussion of the results and their implications in Sec. VI.

II. Canonical Flexible Spacecraft Model

The classical approach for attitude control system (ACS) analysis and design reduces complex flexible spacecraft dynamics into three decoupled, single-axis modal models, one for rotation about each axis (roll, pitch, and yaw) [17, 18]. Each model includes a single rigid body mode and one or more dynamically significant elastic modes. In particular, preliminary analysis and design often rely on single-mode models, i.e., single-axis modal models with a single retained elastic mode. This is the simplest structural dynamic model that includes both rigid body and flexible modes, and hence, is taken as the canonical model for flexible spacecraft dynamics. The canonical model takes the form of the unrestrained spring-mass-damper system with two degrees of freedom (DOFs) depicted in Fig. 2.

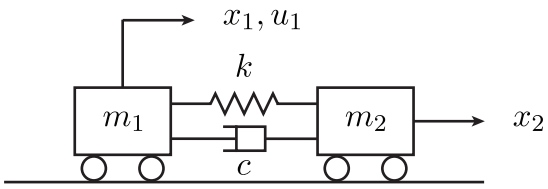

Fig. 2 The canonical model of a flexible spacecraft is a floating spring-mass-damper system with two DOFs.

The equations of motion for the canonical model are

$$\begin{bmatrix} m_1 & 0 \\ 0 & m_2 \end{bmatrix} \begin{bmatrix} \ddot{x}_1 \\ \ddot{x}_2 \end{bmatrix} + \begin{bmatrix} c & -c \\ -c & c \end{bmatrix} \begin{bmatrix} \dot{x}_1 \\ \dot{x}_2 \end{bmatrix} + \begin{bmatrix} k & -k \\ -k & k \end{bmatrix} \begin{bmatrix} x_1 \\ x_2 \end{bmatrix} = \begin{bmatrix} u_1 \\ 0 \end{bmatrix} \tag{1}$$

where m_1 denotes the mass of the spacecraft "bus" with position x_1, m_2 is the mass of the flexible "appendage" with position x_2, k is the spring stiffness, c is the viscous damping coefficient, u_1 is the control input on m_1, and dot notation denotes differentiation with respect to time t. In practice, x_1 is the bus orientation, x_2 is the modal coordinate corresponding to the dominant flexible mode (which is not necessarily the lowest-frequency mode), and u_1 is the attitude control torque. The remaining parameters are related to the rigid and flexible body properties of the spacecraft. Sec. III shows how to reduce arbitrary finite element models into single-axis modal models and, by doing so, derives expressions for these parameters. Importantly, even though the focus of this paper is on attitude slew maneuvers, Eq. (1) applies for either translational or rotational motion. Hence, the parameters and variables in Eq. (1) are to be interpreted in the generalized sense; e.g., m_1 and m_2 are generalized masses that can represent either masses or moments of inertia.

The classical ACS analysis and design approach treats flexibility as a disturbance acting on the spacecraft bus. Thus, the parameter of interest for ACS design and analysis is the influence of m_2 on m_1, not the motion of m_2 itself. To eliminate the motion of m_2, the standard approach is to rewrite Eq. (1) in the Laplace domain and evaluate the transfer function from u_1 to x_1. Taking the Laplace transform of Eq. (1) with zero initial conditions gives

$$m_1 s^2 X_1(s) + cs\left(X_1(s) - X_2(s)\right) + k\left(X_1(s) - X_2(s)\right) = U_1(s) \tag{2}$$

$$m_2 s^2 X_2(s) + cs\left(X_2(s) - X_1(s)\right) + k\left(X_2(s) - X_1(s)\right) = 0 \tag{3}$$

where $X_1(s) = \mathcal{L}(x_1(t))$, $X_2(s) = \mathcal{L}(x_2(t))$, $U_1(s) = \mathcal{L}(u_1(t))$, and $\mathcal{L}(\cdot)$ denotes the Laplace transform that converts a function of time t to a function of the complex frequency s. Solving Eqs. (2) and (3) for $X_1(s)/U_1(s)$, taking a partial fraction expansion, and simplifying yields

$$\frac{X_1(s)}{U_1'(s)} = \frac{1}{s^2} + \frac{m_2/m_1}{s^2 + 2\left(1 + m_2/m_1\right)\zeta\omega_n s + \left(1 + m_2/m_1\right)\omega_n^2} \tag{4}$$

where $\omega_n = \sqrt{k/m_2}$ is the fixed-base natural frequency, $\zeta = c/\left(2\sqrt{km_2}\right)$ is the fixed-base damping ratio (fraction of critical damping), and u_1' is the acceleration input to the system, i.e., $u_1 = (m_1 + m_2)\,u_1'$ [equivalently, $U_1(s) = (m_1 + m_2)\,U_1'(s)$].

Equation (4) consists of two terms, the rigid body translation of m_1 and a perturbation due to the motion of m_2, i.e., due to flexibility. To make this more explicit, let $X_1(s) = X_{1,r}(s) + X_{1,f}(s)$ where the subscripts r and f denote the

rigid body and flexible terms, with corresponding transfer functions

$$\frac{X_{1,r}(s)}{U_1'(s)} = \frac{1}{s^2} \tag{5}$$

$$\frac{X_{1,f}(s)}{U_1'(s)} = \frac{m_2/m_1}{s^2 + 2\left(1 + m_2/m_1\right)\zeta\omega_n s + \left(1 + m_2/m_1\right)\omega_n^2} \tag{6}$$

Taking the inverse Laplace transforms of Eqs. (5) and (6) then gives

$$\ddot{x}_{1,r} = u_1' \tag{7}$$

$$\ddot{x}_{1,f} + 2\left(1 + \frac{m_2}{m_1}\right)\zeta\omega_n\dot{x}_{1,f} + \left(1 + \frac{m_2}{m_1}\right)\omega_n^2 x_{1,f} = \frac{m_2}{m_1}u_1' \tag{8}$$

From Eq. (8), the perturbation due to flexibility (i.e., the flexible dynamics) can be modeled as a damped harmonic oscillator with increased natural frequency $\omega_n\sqrt{1 + m_2/m_1}$ and damping ratio $\zeta\sqrt{1 + m_2/m_1}$ relative to the fixed-base case. The shifted natural frequency $\omega_n\sqrt{1 + m_2/m_1}$ is the free-free natural frequency of Eq. (4).

Classical approaches for flexible spacecraft ACS analysis and design are usually predicated on minimizing the magnitude of any disturbances induced by flexibility, i.e., by making the magnitude of $x_{1,f}$ and its derivatives "small". This entails moving the system sufficiently "slowly" to prevent significant excitation of the flexible mode(s). With this in mind, a standard practice is to require that the closed-loop ACS bandwidth is at least an order of magnitude below the free-free natural frequency $\omega_n\sqrt{1 + m_2/m_1}$ [17].* In this case, the ACS reacts at least an order of magnitude slower than the natural time scale of the system's dynamics. Using this approach, it is often possible to neglect flexibility in ACS design and instead simply design a control system for the rigid body motion, as is done, e.g., in [19].

A similar philosophy is usually adopted for designing slew maneuvers. A nominally rest-to-rest slew maneuver for a rigid spacecraft, i.e., a spacecraft that can be modeled as a rigid body, leads to residual structural vibrations for a flexible one. In light of Eq. (4), the spacecraft bus perceives these vibrations as angular position and velocity errors, the magnitudes of which often appear in ACS pointing error budgets (see e.g., [20]) and are a proxy for pointing stability and jitter. Here, jitter refers to the classical definition of unwanted mechanical vibrations, as opposed to more nuanced definitions typically used for space-borne optical systems [21, 22]. A flexible spacecraft ACS with its closed-loop bandwidth set an order of magnitude below its lowest flexible-mode frequency is incapable of rejecting jitter [17]. For these reasons, minimizing jitter is imperative for pointing accuracy and stability.

A common heuristic for minimizing jitter states that the slew maneuver duration T must be at least an order of magnitude longer than the natural period $T_n = 2\pi/\omega_n$. However, such a requirement is shown to be misguided in Secs. IV and V. In particular, "slow" is relative, and depends on both the "shape" of the forcing applied to the system and the ratio T/T_n. With this in mind, this paper instead proposes using quantitative requirements on the residual (i.e., post-slew) amplitude of $x_{1,f}$ and its derivatives (specifically, on $\dot{x}_{1,f}$) to calculate feasible slew times. For a given spacecraft and slew maneuver, specifying a requirement on the residual amplitude of $x_{1,f}$ or any of its derivatives indirectly specifies a requirement on the minimum slew time. Hedgepeth [23] uses similar arguments to determine a first-mode natural frequency requirement for slewing flexible spacecraft, although his approach underpredicts the amplitudes of $x_{1,f}$ and its derivatives; for additional details, see [8].

III. Derivation of Single-Axis Modal Models

Practical applications of the canonical flexible spacecraft model require relationships between the parameters m_1, m_2, ζ, ω_n, and a flexible spacecraft finite element model. To that end, this section uses the Craig-Bampton method [16] to rigorously and systematically derive single-axis modal models analogous to the canonical model from unrestrained (free-free) finite element models. In doing so, it derives a fully coupled 6-DOF generalization of the transfer function from u_1 to x_1 [Eq. (4)] and shows that the correct set of vibration modes for ACS analysis and design are the Craig-Bampton method's fixed-interface normal modes. It also discusses methods for identifying the most dynamically significant mode(s) and special considerations for symmetric structures. The Craig-Bampton method generalizes the notion of a "bus" with a flexible "appendage" to arbitrarily complex flexible spacecraft.

*In practice, this depends on the spacing of the structural modes. For a system with a few well-separated modes, it is possible to achieve higher bandwidth linear control systems by filtering the structural modes (see e.g., [18] and the references therein). However, this becomes difficult, if not impossible for large space structures with many closely spaced modes (see e.g., [19]), in which case the aforementioned requirement on closed-loop bandwidth becomes imperative.

A. 6-DOF Transfer Function

The derivation of the 6-DOF generalization of the transfer function from u_1 to x_1 [Eq. (4)] starts from the standard equation of motion for a free-free linear finite element model:

$$\mathbf{M}\ddot{\mathbf{x}} + \mathbf{C}\dot{\mathbf{x}} + \mathbf{K}\mathbf{x} = \mathbf{B}\mathbf{u} \tag{9}$$

Here, $\mathbf{x} \in \mathbb{R}^n$ contains the nodal displacement DOFs, $\mathbf{u} \in \mathbb{R}^m$ contains the external forces and moments, $\mathbf{M} \in \mathbb{R}^{n\times n}$ is the symmetric positive definite mass matrix, $\mathbf{C} \in \mathbb{R}^{n\times n}$ is the symmetric positive semi-definite damping matrix, $\mathbf{K} \in \mathbb{R}^{n\times n}$ is the symmetric positive semi-definite stiffness matrix, and $\mathbf{B} \in \mathbb{R}^{n\times m}$ maps the external forces and moments to the nodal DOFs. In general, each node has six DOFs, three translations and three rotations, from which it follows that Eq. (9) admits six rigid body modes. The damping model (e.g., Rayleigh or modal) determines the rank deficiency of $\mathbf{C}$; the number of rigid body modes corresponds to the rank deficiency of $\mathbf{K}$.

For the Craig-Bampton method [16], Eq. (9) is partitioned into n_I interior (I) and n_B boundary (B) coordinates, as follows:

$$\begin{bmatrix} \mathbf{M}_{II} & \mathbf{M}_{IB} \\ \mathbf{M}_{BI} & \mathbf{M}_{BB} \end{bmatrix} \begin{bmatrix} \ddot{\mathbf{x}}_I \\ \ddot{\mathbf{x}}_B \end{bmatrix} + \begin{bmatrix} \mathbf{C}_{II} & \mathbf{C}_{IB} \\ \mathbf{C}_{BI} & \mathbf{C}_{BB} \end{bmatrix} \begin{bmatrix} \dot{\mathbf{x}}_I \\ \dot{\mathbf{x}}_B \end{bmatrix} + \begin{bmatrix} \mathbf{K}_{II} & \mathbf{K}_{IB} \\ \mathbf{K}_{BI} & \mathbf{K}_{BB} \end{bmatrix} \begin{bmatrix} \mathbf{x}_I \\ \mathbf{x}_B \end{bmatrix} = \begin{bmatrix} \mathbf{0}_{n_I\times 1} \\ \mathbf{u}_B \end{bmatrix} \tag{10}$$

where $\mathbf{0}_{n_I\times 1} \in \mathbb{R}^{n_I}$ is a zero vector and $n = n_I + n_B$. Typically, the B-set contains DOFs either shared with adjacent components (when the Craig-Bampton substructure is a component of a larger structural dynamic model) or loaded by external forces or moments; the remaining DOFs belong to the I-set [16]. For a flexible spacecraft, the B-set coordinates are the six rigid body DOFs of the bus, and hence, correspond to x_1 from the canonical model [Eq. (1)]. The I-set coordinates (or the corresponding modal coordinates) are then analogous to x_2 in Eq. (1). With the B-set coordinates defined in this way, $\mathbf{K}_{II}$ is the full-rank stiffness matrix corresponding to fixed (clamped) boundary conditions at the bus. $\mathbf{u}_B$ then contains the forces (e.g., due to thrusters) and moments (e.g., due to the ACS) acting on the bus. Equation (10) is simply a permutation of the rows and columns of Eq. (9).

Following Sec. II, the immediate goal is to derive the transfer function $\mathbf{H}(s)$ that relates a force or moment on B to the corresponding translations and rotations, i.e., to find $\mathbf{H}(s) = \mathbf{G}^{-1}(s)$ such that $\mathbf{X}_B(s) = \mathbf{H}(s)\mathbf{U}_B(s)$ where $\mathbf{X}_B(s) = \mathcal{L}(\mathbf{x}_B(t))$ and $\mathbf{U}_B(s) = \mathcal{L}(\mathbf{u}_B(t))$. $\mathbf{H}(s)$ is subsequently simplified for the special case of a single-axis slew to obtain an expression analogous to Eq. (4). The derivation of $\mathbf{G}(s)$ closely follows the procedure in [24, p. 187–190] for the undamped sinusoidal (steady-state) transfer function $\mathbf{G}(j\omega)$ (referred to as "mechanical impedance" in [24]) where $j^2 = -1$ and ω is the frequency of the harmonic forcing.

The derivation of $\mathbf{G}(s)$ requires taking the Laplace transform of Eq. (10) (again with zero initial conditions), from which it follows that

$$\left(s^2 \begin{bmatrix} \mathbf{M}_{II} & \mathbf{M}_{IB} \\ \mathbf{M}_{BI} & \mathbf{M}_{BB} \end{bmatrix} + s \begin{bmatrix} \mathbf{C}_{II} & \mathbf{C}_{IB} \\ \mathbf{C}_{BI} & \mathbf{C}_{BB} \end{bmatrix} + \begin{bmatrix} \mathbf{K}_{II} & \mathbf{K}_{IB} \\ \mathbf{K}_{BI} & \mathbf{K}_{BB} \end{bmatrix} \right) \begin{bmatrix} \mathbf{X}_I(s) \\ \mathbf{X}_B(s) \end{bmatrix} = \begin{bmatrix} \mathbf{0}_{n_I\times 1} \\ \mathbf{U}_B(s) \end{bmatrix} \tag{11}$$

where $\mathbf{X}_I(s) = \mathcal{L}(\mathbf{x}_I(t))$. Solving the first equation in Eq. (11) for $\mathbf{X}_I(s)$ and substituting this result into the second equation then yields

$$\mathbf{G}(s) = s^2\mathbf{M}_{BB} + s\mathbf{C}_{BB} + \mathbf{K}_{BB} - \mathbf{Z}_{BI}(s)\mathbf{Z}_{II}^{-1}(s)\mathbf{Z}_{IB}(s) \tag{12}$$

where $\mathbf{Z}_{kl}(s) = s^2\mathbf{M}_{kl} + s\mathbf{C}_{kl} + \mathbf{K}_{kl}$. Equation (12) obscures the modal properties of the structure, and hence, is rewritten explicitly in terms of mode shapes and natural frequencies next. Truncating the resulting modal expansion yields a reduced-order modal model.

The fixed-interface normal modes, i.e., the eigenmodes corresponding to fixed (clamped) boundary DOFs, are the solutions to the following generalized eigenproblem [16]:

$$\mathbf{K}_{II}\boldsymbol{\phi}_i = \omega_i^2\mathbf{M}_{II}\boldsymbol{\phi}_i \tag{13}$$

Each fixed-interface normal mode ϕ_i (for $i = 1, \ldots, n_I$) is orthogonal to $\mathbf{M}_{II}$ and normalized such that $\boldsymbol{\phi}_i^T\mathbf{M}_{II}\boldsymbol{\phi}_j = \delta_{ij}$.[†] The n_I solutions to Eq. (13) can equivalently be written in the form

$$\mathbf{K}_{II}\boldsymbol{\Phi} = \mathbf{M}_{II}\boldsymbol{\Phi}\boldsymbol{\Omega}^2 \tag{14}$$

[†] δ_{ij} is the Kronecker delta symbol defined such that $\delta_{ij} = 1$ for $i = j$ and $\delta_{ij} = 0$ otherwise.

where $\boldsymbol{\Phi} = \left(\boldsymbol{\phi}_1, \ldots, \boldsymbol{\phi}_{n_I}\right)$ is the matrix of generalized eigenvectors and $\boldsymbol{\Omega}^2 = \text{diag}\left\{\omega_1^2, \ldots, \omega_{n_I}^2\right\}$. Since each $\boldsymbol{\phi}_i$ is orthogonal with respect to $\mathbf{M}_{II}$,

$$\boldsymbol{\Phi}^T \mathbf{M}_{II} \boldsymbol{\Phi} = \mathbf{I}_{n_I \times n_I} \tag{15}$$

$$\boldsymbol{\Phi}^T \mathbf{K}_{II} \boldsymbol{\Phi} = \boldsymbol{\Omega}^2 \tag{16}$$

where $\mathbf{I}_{n_I \times n_I} \in \mathbb{R}^{n_I \times n_I}$ is an identity matrix. Subsequent developments additionally assume that

$$\boldsymbol{\Phi}^T \mathbf{C}_{II} \boldsymbol{\Phi} = 2\mathbf{Z}\boldsymbol{\Omega} \tag{17}$$

where $\mathbf{Z} = \text{diag}\left\{\zeta_1, \ldots, \zeta_{n_I}\right\}$ is the matrix of modal damping coefficients and $\zeta_i \geq 0$ for all $i = 1, \ldots, n_I$.

The n_I generalized eigenvectors are linearly independent, i.e., $\boldsymbol{\Phi}$ is invertible. Hence, rearranging Eqs. (15)–(17) results in the following identities:

$$\mathbf{M}_{II} = \boldsymbol{\Phi}^{-T} \boldsymbol{\Phi}^{-1} \tag{18}$$

$$\mathbf{K}_{II} = \boldsymbol{\Phi}^{-T} \boldsymbol{\Omega}^2 \boldsymbol{\Phi}^{-1} \tag{19}$$

$$\mathbf{C}_{II} = 2\boldsymbol{\Phi}^{-T} \mathbf{Z}\boldsymbol{\Omega} \boldsymbol{\Phi}^{-1} \tag{20}$$

Inverting $\mathbf{M}_{II}$ and $\mathbf{K}_{II}$ then yields the following modal expansions [24, p. 187–190]:

$$\mathbf{M}_{II}^{-1} = \boldsymbol{\Phi}\boldsymbol{\Phi}^T = \sum_{i=1}^{n_I} \boldsymbol{\phi}_i \boldsymbol{\phi}_i^T \tag{21}$$

$$\mathbf{K}_{II}^{-1} = \boldsymbol{\Phi}\boldsymbol{\Omega}^{-2}\boldsymbol{\Phi}^T = \sum_{i=1}^{n_I} \frac{\boldsymbol{\phi}_i \boldsymbol{\phi}_i^T}{\omega_i^2} \tag{22}$$

from which it readily follows that

$$\mathbf{K}_{II}^{-1} \mathbf{M}_{II} \mathbf{K}_{II}^{-1} = \boldsymbol{\Phi}\boldsymbol{\Omega}^{-4}\boldsymbol{\Phi}^T = \sum_{i=1}^{n_I} \frac{\boldsymbol{\phi}_i \boldsymbol{\phi}_i^T}{\omega_i^4} \tag{23}$$

By analogy with Eq. (23),

$$\mathbf{K}_{II}^{-1} \mathbf{C}_{II} \mathbf{K}_{II}^{-1} = \boldsymbol{\Phi}\boldsymbol{\Omega}^{-2} \left(2\mathbf{Z}\boldsymbol{\Omega}\right) \boldsymbol{\Omega}^{-2}\boldsymbol{\Phi}^T = \sum_{i=1}^{n_I} \frac{\boldsymbol{\phi}_i \left(2\zeta_i\omega_i\right) \boldsymbol{\phi}_i^T}{\omega_i^4} \tag{24}$$

Substituting Eqs. (18)–(20) into $\mathbf{Z}_{II}^{-1}(s)$ then yields

$$\mathbf{Z}_{II}^{-1}(s) = \boldsymbol{\Phi} \left(s^2 \mathbf{I}_{n_I \times n_I} + 2s\mathbf{Z}\boldsymbol{\Omega} + \boldsymbol{\Omega}^2\right)^{-1} \boldsymbol{\Phi}^T \tag{25}$$

which is equivalent to the following modal expansion:

$$\mathbf{Z}_{II}^{-1}(s) = \sum_{i=1}^{n_I} \frac{\boldsymbol{\phi}_i \boldsymbol{\phi}_i^T}{s^2 + 2\zeta_i\omega_i s + \omega_i^2} \tag{26}$$

Further simplifications require the identity [24, p. 189]

$$\frac{1}{s^2 + \omega_i^2} = \frac{1}{\omega_i^2} - \frac{s^2}{\omega_i^4} + \frac{s^4}{\omega_i^4 \left(s^2 + \omega_i^2\right)} \tag{27}$$

and the substitution $s^2 \rightarrow s^2 + 2\zeta_i\omega_i s$. Using Eq. (27) to expand the denominator in Eq. (26) and simplifying with Eqs. (22)–(24) then gives

$$\mathbf{Z}_{II}^{-1}(s) = \mathbf{K}_{II}^{-1} - s^2 \mathbf{K}_{II}^{-1} \mathbf{M}_{II} \mathbf{K}_{II}^{-1} - s\mathbf{K}_{II}^{-1} \mathbf{C}_{II} \mathbf{K}_{II}^{-1} + \sum_{i=1}^{n_I} \frac{\boldsymbol{\phi}_i \left(s^2 + 2\zeta_i\omega_i s\right)^2 \boldsymbol{\phi}_i^T}{\omega_i^4 \left(s^2 + 2\zeta_i\omega_i s + \omega_i^2\right)} \tag{28}$$

Substituting Eq. (28) into Eq. (12) and simplifying ultimately results in the following expression for $\mathbf{G}(s)$:

$$\mathbf{G}(s) = s^2\mathbf{M}^*_{BB} + s\mathbf{C}^*_{BB} + \mathbf{K}^*_{BB} - s^2 \sum_{i=1}^{n_I} \frac{(\mathbf{e}_i + s\mathbf{f}_i)\,(\mathbf{e}_i + s\mathbf{f}_i)^T}{\omega_i^4\left(s^2 + 2\zeta_i\omega_i s + \omega_i^2\right)} \tag{29}$$

where $\mathbf{e}_i = \left(2\zeta_i\omega_i\mathbf{K}_{BI} - \omega_i^2\mathbf{C}_{BI}\right)\boldsymbol{\phi}_i$ and $\mathbf{f}_i = \left(\mathbf{K}_{BI} - \omega_i^2\mathbf{M}_{BI}\right)\boldsymbol{\phi}_i$ are modal vectors and

$$\mathbf{M}^*_{BB} = \mathbf{M}_{BB} - \mathbf{M}_{BI}\mathbf{K}_{II}^{-1}\mathbf{K}_{IB} - \mathbf{K}_{BI}\mathbf{K}_{II}^{-1}\mathbf{M}_{IB} + \mathbf{K}_{BI}\mathbf{K}_{II}^{-1}\mathbf{M}_{II}\mathbf{K}_{II}^{-1}\mathbf{K}_{IB} \tag{30}$$

$$\mathbf{K}^*_{BB} = \mathbf{K}_{BB} - \mathbf{K}_{BI}\mathbf{K}_{II}^{-1}\mathbf{K}_{IB} \tag{31}$$

$$\mathbf{C}^*_{BB} = \mathbf{C}_{BB} - \mathbf{C}_{BI}\mathbf{K}_{II}^{-1}\mathbf{K}_{IB} - \mathbf{K}_{BI}\mathbf{K}_{II}^{-1}\mathbf{C}_{IB} + \mathbf{K}_{BI}\mathbf{K}_{II}^{-1}\mathbf{C}_{II}\mathbf{K}_{II}^{-1}\mathbf{K}_{IB} \tag{32}$$

The derivation of Eq. (29) is conceptually straightforward, but the details are involved and are left to [8]. Equation (29) emphasizes that a force or moment on B induces both rigid body and elastic motions. In practice, it is advantageous to precompute $\mathbf{e}_i$ and $\mathbf{f}_i$ to avoid unnecessary calculations of computationally expensive matrix-vector products during repeated evaluations of Eq. (29).

If the n_B boundary DOFs fully restrain the structure's n_B rigid body modes, then $\mathbf{M}^*_{BB}$ is the rigid body mass matrix of the unrestrained and undeformed structure (evaluated with respect to B) and $\mathbf{K}^*_{BB}$ is the projection of the unrestrained stiffness matrix $\mathbf{K}$ onto the rigid body modes, i.e., $\mathbf{K}^*_{BB} = \mathbf{0}_{n_B\times n_B}$ (otherwise, $\mathbf{K}^*_{BB}$ is singular but non-zero). The properties of $\mathbf{C}^*_{BB}$ depend on the damping model. A particularly convenient choice for the damping model is stiffness-proportional damping, in which case $\mathbf{C} = (2\zeta_1/\omega_1)\mathbf{K}$ where ω_1 and ζ_1 are respectively the first-mode natural frequency and damping ratio. With stiffness-proportional damping, higher-frequency modes are more heavily damped; specifically, $\zeta_i = \zeta_1(\omega_i/\omega_1)$ for $i = 1, \ldots, n_I$. Thus, $\mathbf{C}^*_{BB} = \mathbf{0}_{n_B\times n_B}$ and $\mathbf{e}_i = \mathbf{0}_{n_B\times 1}$. Together, these assumptions reduce Eq. (29) to

$$\mathbf{G}(s) = s^2\mathbf{M}^*_{BB} - s^4 \sum_{i=1}^{n_I} \frac{\mathbf{f}_i\mathbf{f}_i^T}{\omega_i^4\left(s^2 + 2\zeta_i\omega_i s + \omega_i^2\right)} \tag{33}$$

Equation (33) is equivalent to Eq. (8.21) in [24] when $s = j\omega$ and $\zeta_i = 0$ for $i = 1, \ldots, n_I$.

The modal participation vector $\mathbf{f}_i$ is related to the dynamic reaction of the ith mode on B due to an external force or moment on B [24, p. 187–190]. The corresponding modal mass matrix $\mathbf{M}_i = \mathbf{f}_i\mathbf{f}_i^T/\omega_i^4$ determines the flexible body accelerations required to dynamically react an external force or moment on B and how those accelerations are distributed among the eigenmodes. The total modal mass matrix is

$$\sum_{i=1}^{n_I} \mathbf{M}_i = \mathbf{K}_{BI}\mathbf{K}_{II}^{-1}\mathbf{M}_{II}\mathbf{K}_{II}^{-1}\mathbf{K}_{IB} - \mathbf{K}_{BI}\mathbf{K}_{II}^{-1}\mathbf{M}_{IB} - \mathbf{M}_{BI}\mathbf{K}_{II}^{-1}\mathbf{K}_{IB} + \mathbf{M}_{BI}\mathbf{M}_{II}^{-1}\mathbf{M}_{IB} \tag{34}$$

which is derived from $\mathbf{M}_i = \mathbf{f}_i\mathbf{f}_i^T/\omega_i^4$ and Eqs. (21)–(23). Equation (34) is only a function of the finite element mass and stiffness matrices, i.e., it is independent of the computed eigenmodes.

A closed-form expression for the transfer function $\mathbf{H}(s) = \mathbf{G}^{-1}(s)$ can be derived using the Woodbury matrix identity [25], or equivalently, repeated applications of the Sherman-Morrison formula [25] (see also [26]). The latter is useful for developing reduced-order models with only a handful of retained modes because it results in explicit relationships for the modal interactions.

Using the Woodbury matrix identity to invert $\mathbf{G}(s)$ requires rewriting the modal expansion in Eq. (33) as a matrix product. To do this, let $\boldsymbol{\Lambda}(s) = \text{diag}\left\{s^2 + 2\zeta_1\omega_1 s + \omega_1^2, \ldots, s^2 + 2\zeta_{n_I}\omega_{n_I} s + \omega_{n_I}^2\right\}$ and $\mathbf{F} = \left(\mathbf{f}_1/\omega_1^2, \ldots, \mathbf{f}_{n_I}/\omega_{n_I}^2\right)$, from which it follows that $\mathbf{G}(s)$ can be written as

$$\mathbf{G}(s) = s^2\mathbf{M}^*_{BB} - s^4\mathbf{F}\boldsymbol{\Lambda}^{-1}(s)\mathbf{F}^T \tag{35}$$

Applying the Woodbury matrix identity then results in the following exact expression for $\mathbf{H}(s) = \mathbf{G}^{-1}(s)$:

$$\mathbf{H}(s) = \frac{1}{s^2}\mathbf{M}^{*-1}_{BB} + \mathbf{M}^{*-1}_{BB}\mathbf{F}\left(\boldsymbol{\Lambda}(s) - s^2\mathbf{F}^T\mathbf{M}^{*-1}_{BB}\mathbf{F}\right)^{-1}\mathbf{F}^T\mathbf{M}^{*-1}_{BB} \tag{36}$$

This is the 6-DOF generalization of the transfer function from u_1 to x_1 from Sec. II [Eq. (4)]. Equation (36) is subsequently specialized for the case of a single-axis, single-mode model in Sec. III.C.

B. Mode Selection Criteria

Following [24, p. 191–192], Eq. (33) shows how to select "dominant" eigenmodes for general reduced-order models, i.e., which modes to retain in a truncated modal expansion. Specifically, $\mathbf{f}_i$ measures the modal participation of mode i; the larger the magnitude of $\mathbf{f}_i$, the larger the dynamic reaction on B, the larger the modal mass, and the more dominant the mode. For these reasons, [24] suggests using the magnitude of the ith term in the modal expansion from Eq. (33) to rank modes from most dominant to least dominant:

$$p_i = ||\mathbf{f}_i/\omega_i^2||_2^2 = \operatorname{tr}\mathbf{M}_i \tag{37}$$

Here, $||\cdot||_2$ denotes the Euclidean norm. Larger values of p_i correspond to more dominant modes. The ω_i^4 in the denominator of Eq. (37) implies that dominant modes tend to be lower-frequency modes, but in general, the dominant mode is not necessarily the lowest-frequency mode.

Equation (37) is ill-defined for structures with both translational and rotational DOFs. To remedy this, the coordinate partition from [27] is used to develop a modified mode selection criterion. Specifically, $\mathbf{f}_i$ is partitioned into translational (T) and rotational (R) DOFs such that $\mathbf{f}_i^T = \left(\mathbf{f}_{i,T}^T, \mathbf{f}_{i,R}^T\right)$. The modes are then sorted according to the following criterion:

$$q_i = \frac{1}{2}\left(\frac{||\mathbf{f}_{i,T}/\omega_i^2||_2^2}{\sum_{i=1}^{n_I}||\mathbf{f}_{i,T}/\omega_i^2||_2^2} + \frac{||\mathbf{f}_{i,R}/\omega_i^2||_2^2}{\sum_{i=1}^{n_I}||\mathbf{f}_{i,R}/\omega_i^2||_2^2}\right) \tag{38}$$

where $\mathbf{f}_{i,T}\mathbf{f}_{i,T}^T/\omega_i^4$ and $\mathbf{f}_{i,R}\mathbf{f}_{i,R}^T/\omega_i^4$ are the translational and rotational blocks of the modal mass matrix $\mathbf{M}_i$, the summations in the denominators are evaluated using Eq. (34), and again larger values correspond to more dominant modes. Equation (38) is the average of the ith mode's translational modal mass (normalized by the total modal mass) and rotational modal inertia (normalized by the total modal inertia). Equivalently, it is a normalized measure of the ith mode's dynamic reaction on B. For models with either translational DOFs or rotational DOFs, but not both, Eq. (38) reduces to a normalized version of Eq. (37). Importantly, both Eqs. (37) and (38), and hence, the resulting mode sortings, are invariant to reference frame transformations.

Equation (38) is equivalent to the effective interface mass introduced by Kammer and Triller [27]. Specifically, $\mathbf{M}_i$ is equivalent to their matrix $[\overline{\mathbf{M}}_i]$. This is straightforward to show by expanding $[\overline{\mathbf{M}}_i]$, substituting Eq. (22), and using the orthogonality of $\mathbf{\Phi}$ [Eq. (15)]. With collocated sensors and actuators, effective interface mass, and by extension, Eq. (38), also measures the relative controllability and observability of each fixed-interface mode [28]. The higher the value of Eq. (38), the more controllable and observable the mode. Moreover, effective interface mass is closely related to the balanced singular values [29] from the balanced truncation method of model reduction [30]. For undamped free vibrations, balanced truncation yields normal vibration modes [31].

For a single-axis modal model, the dominant mode is the mode with the maximum modal mass or inertia per axis, i.e., the maximum absolute value in the corresponding DOF in $\mathbf{f}_i$. In general, different modes are dominant for translational and rotational motions about different axes.

Special considerations are required for symmetric structures. These structures have natural frequencies (eigenvalues) with multiplicities greater than one; the actual multiplicity of a given eigenvalue depends on a structure's specific symmetries [32]. Due to the limitations of floating point computations and the accumulation of round-off errors, it is often difficult to distinguish between symmetric modes with repeated eigenvalues and merely closely spaced modes. Conveniently, the same criteria used to sort modes can also be used to identify repeated eigenvalues. In particular, both the magnitude of the modal participation vector $\mathbf{f}_i$ and the trace of the modal mass matrix $\mathbf{M}_i$ are invariant to the operations of a symmetry group. Hence, these quantities are both invariant for symmetric modes, meaning symmetric modes have the same values (to within close numerical tolerances) of both Eq. (37) and Eq. (38). Closely spaced modes, on the other hand, typically have distinct values of both Eq. (37) and Eq. (38). This has important implications for the development of reduced-order models for symmetric structures, as discussed further in Sec. III.D.

C. Reduction to Canonical Model

For the case when only the ith mode is retained in the modal expansion, i.e., the ith mode is the dominant mode, Eq. (36) reduces to

$$\mathbf{H}(s) = \frac{1}{s^2}\mathbf{M}_{BB}^{*-1} + \frac{\mathbf{M}_{BB}^{*-1}\mathbf{M}_i\mathbf{M}_{BB}^{*-1}}{\left(1 - \operatorname{tr}\left(\mathbf{M}_{BB}^{*-1}\mathbf{M}_i\right)\right)s^2 + 2\zeta_i\omega_i s + \omega_i^2} \tag{39}$$

which uses the definition of the modal mass matrix $\mathbf{M}_i = \mathbf{f}_i \mathbf{f}_i^T / \omega_i^4$ and the identity $\mathbf{f}_i^T \mathbf{M}_{BB}^{*-1} \mathbf{f}_i / \omega_i^4 = \text{tr}\left(\mathbf{M}_{BB}^{*-1} \mathbf{M}_i\right)$. In turn, the relationship between $\mathbf{X}_B(s)$ and $\mathbf{U}'_B(s)$ takes the form

$$\mathbf{X}_B(s) = \left(\frac{1}{s^2} \mathbf{I}_{n_B \times n_B} + \frac{\mathbf{M}_{BB}^{*-1} \mathbf{M}_i}{\left(1 - \text{tr}\left(\mathbf{M}_{BB}^{*-1} \mathbf{M}_i\right)\right) s^2 + 2\zeta_i \omega_i s + \omega_i^2} \right) \mathbf{U}'_B(s) \tag{40}$$

where $\mathbf{U}_B(s) = \mathbf{M}_{BB}^* \mathbf{U}'_B(s)$. Aside from the modal truncation, Eqs. (39) and (40) are both exact.

From here, several assumptions are required to reduce Eq. (40) to a form analogous to the canonical model [Eq. (4)]. Such a model relates the response of a generalized displacement $X_{B,j}(s)$ to the corresponding scalar control input $U'_{B,j}(s)$ for some $j = 1, \ldots, n_B$. For this reason, $\mathbf{U}'_B(s)$ is restricted to a generalized acceleration input about a single axis, i.e., $\mathbf{U}'(s) = \mathbf{e}_j U'_{B,j}(s)$ where $\mathbf{e}_j$ is a standard unit basis vector in $\mathbb{R}^{n_B}$. Similarly, the generalized displacement $\mathbf{X}_B(s)$ is restricted to a translation or rotation about a single axis by left-multiplying both sides of Eq. (40) by $\mathbf{e}_j^T$, i.e., $X_{B,j}(s) = \mathbf{e}_j^T \mathbf{X}_B(s)$. Additional assumptions decouple the B-set coordinates. In particular, it is assumed that the B-set coordinates correspond to a node located at the structure's undeformed center of mass and that the global finite element reference frame coincides with principal inertial axes. These assumptions diagonalize $\mathbf{M}_{BB}^*$. It follows that

$$\frac{X_{B,j}(s)}{U'_{B,j}(s)} = \frac{1}{s^2} + \frac{M_{i,jj} / M_{BB,jj}^*}{\left(1 - \text{tr}\left(\mathbf{M}_{BB}^{*-1} \mathbf{M}_i\right)\right) s^2 + 2\zeta_i \omega_i s + \omega_i^2} \tag{41}$$

where the subscript jj denotes the jth main diagonal entry of the corresponding matrix. Lastly, it is assumed that $\text{tr}\left(\mathbf{M}_{BB}^{*-1} \mathbf{M}_i\right) \approx M_{i,jj} / M_{BB,jj}^*$, i.e., the matrix $\mathbf{M}_{BB}^{*-1} \mathbf{M}_i$ has a single dominant main diagonal term. With this assumption, Eq. (41) simplifies to

$$\frac{X_{B,j}(s)}{U'_{B,j}(s)} = \frac{1}{s^2} + \frac{\eta_{jj}}{s^2 + 2\left(1 + \eta_{jj}\right) \zeta_i \omega_i s + \left(1 + \eta_{jj}\right) \omega_i^2} \tag{42}$$

with mass ratio

$$\eta_{jj} = \frac{M_{i,jj}}{M_{BB,jj}^* - M_{i,jj}} \tag{43}$$

Comparing Eqs. (42) and (4) reveals that $m_1 = M_{BB,jj}^* - M_{i,jj}$, i.e., the *difference* between the rigid body mass and the modal mass, not the rigid body mass itself; $m_2 = M_{i,jj}$; $\zeta = \zeta_i$; and $\omega_n = \omega_i$. Thus, the parameters in the canonical model are related to the rigid body mass and the dominant mode's modal mass, damping ratio, and natural frequency (where again "mass" is to be interpreted in the generalized sense of either translational or rotational inertia)

D. Canonical Model for Symmetric Structures

The derivation of single-axis modal models requires special considerations when the dominant eigenmode corresponds to a repeated eigenvalue. This is particularly important for flexible spacecraft with symmetric structural architectures. The analysis that follows specifically considers 4-fold symmetric structures, a class of structures that includes solar sails and the Caltech SSPP spacecraft [6], but the approach and conclusions readily generalize to structures with other symmetries. 4-fold symmetric structures have eigenvalues with multiplicities of either one or two [32].

When the dominant eigenmode corresponds to a repeated eigenvalue, Eq. (42) underpredicts the magnitude of the elastic disturbance on the spacecraft bus. Instead of truncating the modal expansion after the dominant mode, the correct truncation includes both the dominant mode (assumed to be the ith mode with natural frequency ω_i) and the associated symmetric mode (assumed to be the $(i+1)$th mode with natural frequency $\omega_{i+1} = \omega_i$). In this case, $\mathbf{f}_i = \mathbf{T}\mathbf{f}_{i+1}$ where $\mathbf{T}$ is an orthogonal matrix corresponding to a symmetry operation [32]. Assuming both modes share the same damping ratio $\zeta_i = \zeta_{i+1}$, then the truncated form of Eq. (36) is

$$\mathbf{H}(s) = \frac{1}{s^2} \mathbf{M}_{BB}^{*-1} + \frac{\mathbf{M}_{BB}^{*-1} \left(\mathbf{M}_i + \mathbf{M}_{i+1}\right) \mathbf{M}_{BB}^{*-1}}{\left(1 - \text{tr}\left(\mathbf{M}_{BB}^{*-1} \mathbf{M}_i\right)\right) s^2 + 2\zeta_i \omega_i s + \omega_i^2} \tag{44}$$

the derivation of which uses $\mathbf{f}_i = \mathbf{T}\mathbf{f}_{i+1}$; the invariance of the rigid body mass matrix $\mathbf{M}_{BB}^*$ to symmetry operations, i.e., $\mathbf{M}_{BB}^* = \mathbf{T}^T \mathbf{M}_{BB}^* \mathbf{T}$; the definition of the modal mass matrix $\mathbf{M}_i = \mathbf{f}_i \mathbf{f}_i^T / \omega_i^4$; and the identity $\mathbf{f}_i^T \mathbf{M}_{BB}^{*-1} \mathbf{f}_i / \omega_i^4 = \text{tr}\left(\mathbf{M}_{BB}^{*-1} \mathbf{M}_i\right)$. The derivation of Eq. (44) additionally assumes that $\mathbf{f}_i^T \mathbf{f}_{i+1} = 0$ (which reflects that the symmetry operation for a 4-fold symmetric structure is a rotation by 90 deg) and that $\mathbf{M}_{BB}^*$ is diagonal with equal inertias about the axes of symmetry.

From here, the reduction to the canonical model [Eq. (4)] mirrors the derivation from Sec. III.C with the caveat that it is now assumed that the matrix $\mathbf{M}_{BB}^{*-1}\mathbf{M}_i$ contains two main diagonal terms of similar magnitudes. Thus, $\text{tr}\left(\mathbf{M}_{BB}^{*-1}\mathbf{M}_i\right) \approx M_{i,jj}/M_{BB,jj}^{*} + M_{i,kk}/M_{BB,kk}^{*}$, which due to symmetry is equivalent to $(M_{i,jj} + M_{i+1,jj})/M_{BB,jj}^{*}$. Since the ith mode is the dominant mode, $M_{i,jj} > M_{i+1,jj}$. With this assumption, the transfer function from $U'_{B,j}(s)$ to $X_{B,j}(s)$ takes the canonical form

$$\frac{X_{B,j}(s)}{U'_{B,j}(s)} = \frac{1}{s^2} + \frac{\eta_{jj}}{s^2 + 2\left(1+\eta_{jj}\right)\zeta_i\omega_i s + \left(1+\eta_{jj}\right)\omega_i^2} \tag{45}$$

where the mass ratio is now given by

$$\eta_{jj} = \frac{M_{i,jj} + M_{i+1,jj}}{M_{BB,jj}^{*} - \left(M_{i,jj} + M_{i+1,jj}\right)} \tag{46}$$

Equivalently,

$$\eta_{jj} = \left(1 + \frac{M_{i+1,jj}}{M_{i,jj}}\right)\frac{M_{i,jj}}{M_{BB,jj}^{*} - \left(M_{i,jj} + M_{i+1,jj}\right)} \tag{47}$$

which shows that the elastic disturbance due to the $(i+1)$th mode is proportional to the ratio between its modal mass $M_{i+1,jj}$ and the dominant mode's modal mass $M_{i,jj}$.

IV. Structure-Based Slew Maneuver Requirements

The canonical flexible spacecraft model from Sec. II (or an analogous reduced-order model from Sec. III) provides a useful tool for developing slew maneuver requirements, i.e., requirements on the ratio T/T_n between the slew maneuver duration T and the fixed-base natural period T_n. To that end, this section first uses a bang-bang slew maneuver to demonstrate that settling time is a poor metric for deriving flexible spacecraft slew maneuver requirements. This motivates the use of a metric based on the amplitude of the residual disturbance due to the flexible dynamics instead. A smooth slew maneuver then highlights how tailoring the "shape" of the slew profile can decrease the excitation of the flexible mode relative to the baseline bang-bang case. The latter is a fairly well-known result in general (see e.g., [33–36]) and is the premise underlying the use of input shaping [37, 38] for reducing residual vibrations, but is less well-used in the definition of flexible spacecraft slew maneuver requirements.

A. Reference Slew Maneuvers

Two reference slew maneuvers are considered in this paper: a bang-bang slew and a smooth polynomial slew, both of which are nominally rest-to-rest maneuvers through a generalized displacement Δx in time T. Their accelerations, velocities, and displacements are depicted in Fig. 3. It is emphasized that these maneuvers are not necessarily appropriate for implementation on actual flight systems. Rather, they are merely intended to illustrate some of the important design considerations associated with slewing flexible spacecraft.

A bang-bang slew is the time-optimal, rest-to-rest, single-axis reorientation maneuver for a rigid body with angular acceleration (torque) constraints [39]. Each "bang" is a step acceleration input of magnitude

$$\ddot{x}_{\max} = \frac{4\Delta x}{T^2} \tag{48}$$

and duration $T/2$, as depicted in Fig. 3a. For a rigid body, the first "bang" linearly accelerates the system from rest to a peak velocity of

$$\dot{x}_{\max} = \frac{\ddot{x}_{\max}T}{2} = \frac{2\Delta x}{T} \tag{49}$$

at time $t = T/2$. The second "bang" then linearly decelerates the system back to rest; see Fig. 3b. The constant magnitude accelerations yield the quadratic variation in the generalized displacement $x(t)$ shown in Fig. 3c.

Comparing the bang-bang and smooth polynomial slew maneuvers emphasizes that both the slew profile and the ratio T/T_n between the slew maneuver duration T and the natural period T_n determine the disturbance due to the flexible dynamics. Following [33], the smooth slew maneuver considered here is based on a higher-order (in this case, 7th-order) polynomial for the generalized displacement $x(t)$:

$$\frac{x(t)}{\Delta x} = -20\left(\frac{t}{T}\right)^7 + 70\left(\frac{t}{T}\right)^6 - 84\left(\frac{t}{T}\right)^5 + 35\left(\frac{t}{T}\right)^4 \tag{50}$$

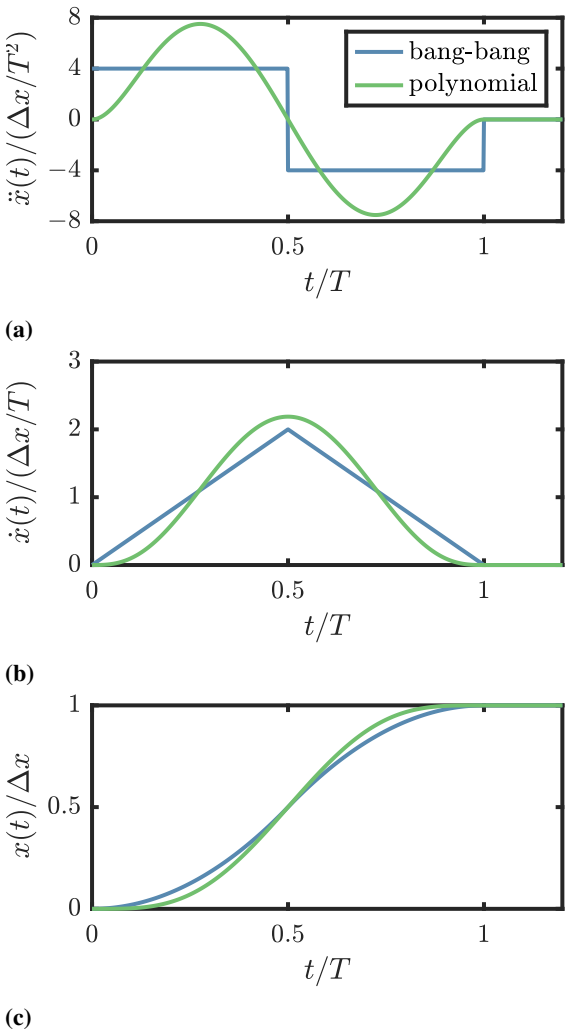

Fig. 3 Comparison of rest-to-rest bang-bang and polynomial slew profiles for rigid spacecraft: (a) accelerations, (b) velocities, and (c) displacements.

This is the lowest-order polynomial that can simultaneous satisfy boundary conditions on $x(t)$ and its velocity, acceleration, and jerk (the time derivative of the acceleration). The polynomial coefficients in Eq. (50) correspond to a rest-to-rest slew through a generalized displacement Δx in time T with zero-velocity, zero-acceleration, and zero-jerk boundary conditions. The zero-jerk boundary conditions reduce jerk by flattening the acceleration curve in the vicinities of the start and end points. Reducing jerk usually reduces the amplitude of the disturbance due to the flexible dynamics [33–36]. Additionally, momentum control systems are usually jerk-limited [36], meaning hardware limitations may also mandate the use of low-jerk slew trajectories. The polynomial slew smoothly accelerates and then decelerates a nominally rigid spacecraft from rest-to-rest.

Compared to the baseline bang-bang slew, the polynomial slew requires higher peak accelerations to achieve the same total displacement in the same time. In this case, the peak acceleration is

$$\ddot{x}_{\max} = \frac{84\sqrt{5}\Delta x}{25T^2} \tag{51}$$

which occurs at times $t = (5 \mp \sqrt{5})T/10$. The peak acceleration is approximately 1.9 times higher than the peak acceleration for the bang-bang slew and leads to proportionally higher peak structural loads. Larger accelerations also

lead to larger velocities. The peak velocity occurs at time $t = T/2$ and is given by

$$\dot{x}_{\max} = \frac{35\Delta x}{16T} \tag{52}$$

This is approximately 1.1 times higher than the peak velocity for the bang-bang slew. Thus, for a given slew time T, the polynomial slew requires a higher average acceleration than the bang-bang slew, which in turn results in proportionally higher average structural loads.

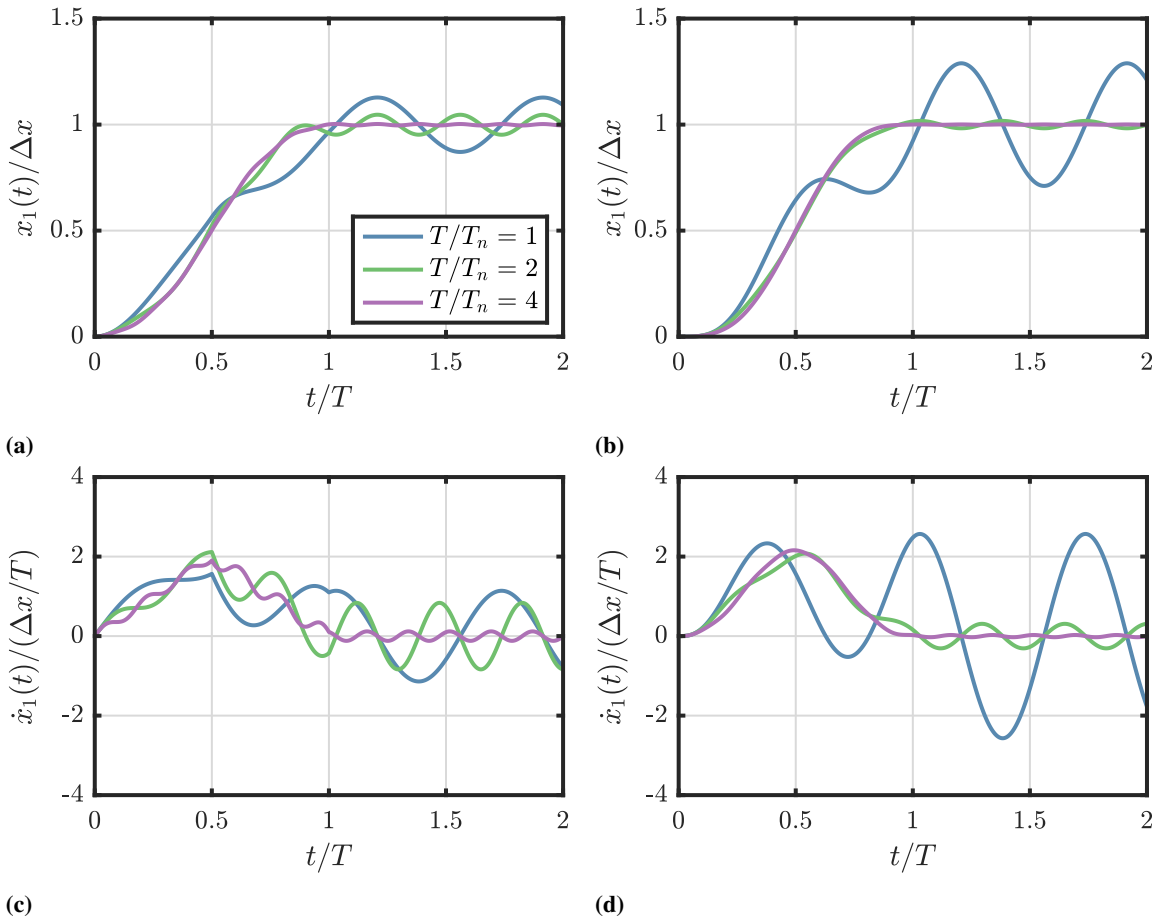

Fig. 4 Transient responses of spacecraft bus for an undamped canonical flexible spacecraft [Eq. 1] with $m_1 = m_2$ during slew maneuvers of duration T. Positions during (a) bang-bang and (b) polynomial slews. Velocities during (c) bang-bang and (d) polynomial slews.

To highlight the differences between a rigid spacecraft and a flexible one, Fig. 4 depicts several representative responses of an undamped canonical flexible spacecraft [Eq. (1)] with $m_1 = m_2$ to bang-bang and polynomial slews. The general trend is that the magnitude of the disturbance due to the flexible dynamics decreases as the duration of the slew increases, i.e., as T/T_n increases. In other words, as T/T_n increases, the responses approach the rigid spacecraft responses from Fig. 3. Compared to the responses to a bang-bang slew, the larger peak accelerations during the polynomial slew result in larger-amplitude transient oscillations for small values of T/T_n, e.g., for $T/T_n = 1$. However, as T/T_n increases, the amplitude of the oscillations decreases faster for the polynomial slew than it does for the bang-bang slew. For example, with $T/T_n = 4$, the response of the flexible spacecraft to the polynomial slew closely approximates the response of the rigid spacecraft from Fig. 3. This implies that there is a critical value of T/T_n beyond which the disturbance due to the flexible dynamics is always smaller for a polynomial slew than it is for a bang-bang slew.

B. Slew Maneuver Requirements Based on Settling Times

The settling time, i.e., the time it takes for the amplitude of oscillation to subside below some specified threshold, is a natural way to specify the minimum slew time for a flexible spacecraft. For second-order linear systems, it is common to define the settling time using either 2% or 5% of the final (steady-state) response to a specified input [40]. 2% is used in what follows.

With its base fixed, i.e., with the constraints $x_1 = 0$ and $\dot{x}_1 = 0$, the canonical flexible spacecraft [Fig. 2] is simply a 1-DOF damped harmonic oscillator. The 2% settling time T_s for a 1-DOF damped harmonic oscillator with natural period $T_n = 2\pi/\sqrt{k/m_2}$ subject to a unit step input is [40]

$$\frac{T_s}{T_n} = \frac{2}{\pi\zeta} \tag{53}$$

where $\zeta = c/\left(2\sqrt{km_2}\right)$ is the damping ratio. From Eq. (53), T_s increases inversely proportionally to ζ.

For a bang-bang slew, the minimum slew time T is twice the settling time T_s, i.e., $T = 2T_s$. In this way, there is sufficient time for the response to settle from both the first "bang" before applying the second "bang" and from the second "bang" before the end of the slew. It follows that the minimum slew time for the canonical flexible spacecraft [Eq. (1)] takes the form

$$\frac{T}{T_n} = \frac{4}{\pi\zeta\,(1 + m_2/m_1)} \tag{54}$$

where T_n and ζ are again its fixed-base natural period and damping ratio. The derivation of Eq. (54) uses $T = 2T_s$ and entails substituting the natural period $T_n/\sqrt{1 + m_2/m_1}$ and damping ratio $\zeta\sqrt{1 + m_2/m_1}$ for the canonical flexible spacecraft from Eq. (8) into Eq. (53). With a settled response, a spacecraft can immediately resume operations like science data collection post-slew.

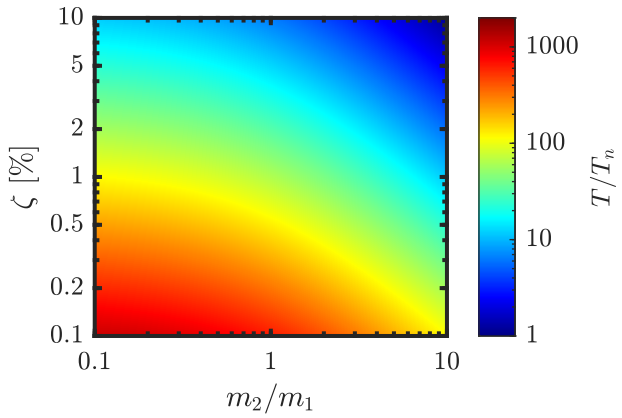

Fig. 5 Minimum bang-bang slew time T derived from the 2% settling time for the canonical flexible spacecraft [Fig. 2] with fixed-base natural period T_n.

Figure 5 plots Eq. (54) as a function of the mass ratio m_2/m_1 and the damping ratio ζ. Based on the figure, the very low damping ratios ($\zeta \ll 1\%$) characteristic of large flexible spacecraft [41] imply settling times that are typically between 100 and 1000 times the fixed-base natural period. For example, with a dominant-mode frequency of 0.1 Hz, $m_2 = m_1$, and 0.5% modal damping, the minimum slew time is approximately 22 min, something comparable to the slew maneuver durations for existing exploration-class NASA spacecraft (e.g., Juno or Europa Clipper) and smaller solar sails (e.g., NEA Scout [42]). The situation, however, progressively deteriorates as flexibility increases and damping decreases. With a dominant-mode frequency of 1 mHz (relevant to some proposed flexible spacecraft concepts, e.g. [6]), $m_2 = m_1$, and 0.2% modal damping, Eq. (54) predicts a minimum slew time in excess of 88 h. Thus, settling times can lead to impractical slew maneuver requirements for very flexible spacecraft.

C. Slew Maneuver Requirements Based on Residual Flexible Dynamics

For a bang-bang slew, the settling time [Eq. (54)] is independent of the magnitude of the step inputs. In light of Fig. 4, the magnitude of the disturbance due to the flexible dynamics decreases as the slew time increases. As a result,

for a sufficiently slow slew, the magnitude of this disturbance can be considered negligible even though Eq. (54) may predict a very long slew time. This implies that a more suitable criterion for determining flexible spacecraft slew maneuver requirements is a metric based on the magnitude of the residual disturbance due to the flexible dynamics. In other words, instead of relying on damping to dissipate the flexible dynamics over time, it is preferable to slew the spacecraft in a way that bounds the residual disturbance due to the flexible dynamics at or below a tolerable level. In what follows, this residual disturbance is evaluated at time T, which for an undamped system is equal to the residual disturbance for all $t \geq T$. The metric for defining what is tolerable depends on the application. The sequel proposes a metric that prioritizes spacecraft pointing performance, but other metrics may be more suitable for other applications, e.g., ones that prioritize shape accuracy.

Slew maneuver loads are generally impulsive, i.e., they are applied over (relatively) short time scales. A structure's peak (worst-case) response to an impulsive load is usually reached before damping can dissipate significant energy [43]. Additionally, spacecraft structures are usually very lightly damped; 0.5% modal damping is typical [41]. For these reasons, it is reasonable to neglect damping for slew maneuver analysis (although the same cannot necessarily be said for ACS analysis and design). The underlying assumption here is that the feasible slew times decrease with damping. In other words, the undamped response provides an upper bound on the feasible slew time.

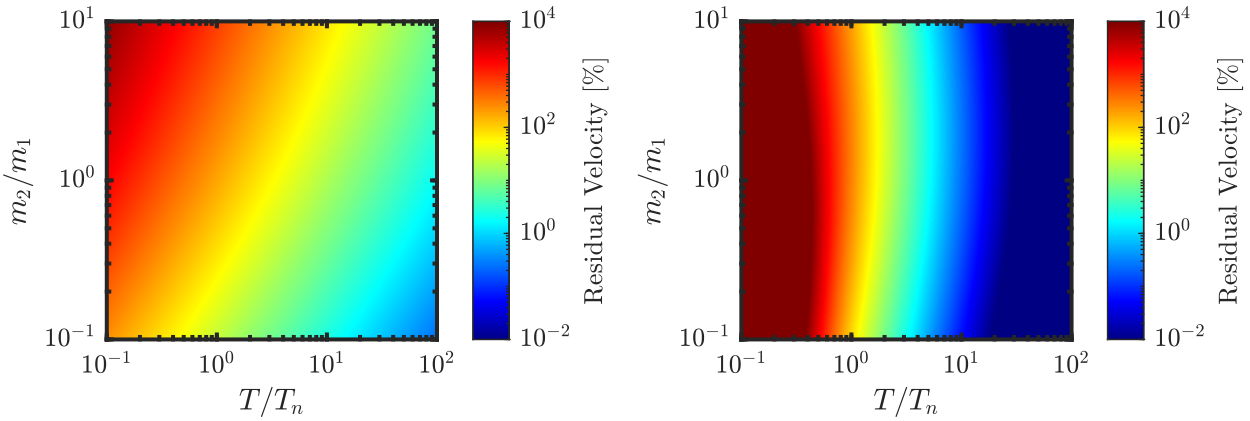

Fig. 6 Amplitude of the residual velocity $|\dot{x}_{1,f}|/(\Delta x/T)$ for (a) bang-bang and (b) polynomial slew maneuvers.

Generally speaking, an ACS can more easily tolerate angular position errors than angular velocity ones. Unlike angular position errors, even small angular velocity errors can lead to unwanted effects, e.g., smearing in optical sensors, that are difficult to correct a posteriori. For this reason, feasible slew times in this paper are calculated from Eq. (8) using requirements on the residual (i.e., post-slew) amplitude of the velocity $\dot{x}_{1,f}$. For a bang-bang slew of the canonical flexible spacecraft, the amplitude of the residual velocity, denoted $|\dot{x}_{1,f}|$, is

$$\frac{|\dot{x}_{1,f}|}{(\Delta x/T)} = \frac{8}{\pi} \frac{m_2/m_1}{\sqrt{1+m_2/m_1}} \left(\frac{T}{T_n}\right)^{-1} \sin^2\left(\frac{\pi}{2}\sqrt{1+m_2/m_1}\left(\frac{T}{T_n}\right)\right) \tag{55}$$

with the upper bound

$$\frac{|\dot{x}_{1,f}|}{(\Delta x/T)} \leq \frac{8}{\pi} \frac{m_2/m_1}{\sqrt{1+m_2/m_1}} \left(\frac{T}{T_n}\right)^{-1} \tag{56}$$

Figure 6a then plots Eq. (56) as a function of both T/T_n and m_2/m_1. An important takeaway is that lower mass ratios and higher slew times result in lower residual velocities. The figure maps the design space of possible values for T/T_n and m_2/m_1 that meet a specified requirement on the residual velocity.

Analogous to Fig. 6a, Fig. 6b plots an upper bound for $|\dot{x}_{1,f}|/(\Delta x/T)$ as a function of T/T_n and m_2/m_1 for the polynomial slew. For $T/T_n > 1$, Fig. 6b demonstrates that the polynomial slew often reduces the amplitude of the residual velocity by two orders of magnitude or more compared to the reference bang-bang slew. In other words, the polynomial slew significantly lowers the excitation of the flexible mode despite its higher peak velocity and acceleration. Thus, for a given spacecraft and requirement on the amplitude of the residual velocity, the polynomial slew achieves significantly faster slews than its bang-bang counterpart.

Equation (56) or the analogous expressions for other slew profiles can be used to rigorously define constraints on slew maneuver performance. For example, given the slew maneuver and the mass ratio m_2/m_1, these types of expressions define the minimum T/T_n that meets a specified requirement on the amplitude of the residual angular velocity. Consequently, there is no universal heuristic for choosing T/T_n; rather, the minimum T/T_n is a function of the application, the spacecraft, and the slew maneuver.

V. Minimum Slew Times for a Flexible Spacecraft

This section uses the methods from Secs. III and IV to study feasible slew times for a representative flexible spacecraft based on the Caltech SSPP spacecraft structural architecture (Fig. 1). The goals of this section are twofold: (i) to demonstrate the use of simple analytical models to predict minimum slew times, and (ii) to verify these slew times using geometrically nonlinear finite element simulations. To that end, this section is organized as follows: Sec. V.A describes the Caltech SSPP spacecraft structural architecture and its finite element implementation; see also Chapter 7 of [8] for more details. Sec. V.B uses reduced-order modal models to predict minimum slew times for SSPP spacecraft at various length scales. Sec. V.C then uses geometrically nonlinear finite element simulations to verify the predicted slew time for a 24 m $\times$ 24 m SSPP spacecraft with a first-mode frequency of approximately 25 mHz. In the context of the Caltech SSPP, a 24 m $\times$ 24 m spacecraft is significantly more flexible than smaller spacecraft (with outer dimensions on the order of 10 m or less), but is less complex and lower risk to design, build, and fly than a full-scale flight system. As a result, such a spacecraft is an intermediate step for demonstrating the requisite attitude dynamics and control technologies before developing a full-scale flight system.

A. Overview of Caltech SSPP Spacecraft Structural Architecture

The flexible spacecraft studied in this section is based on the ultralight, packageable, and self-deployable spacecraft structural architecture originally proposed by the Caltech SSPP for space solar power satellites in [6]; see Fig. 1.

The smallest modular unit in the SSPP architecture has typical maximum dimensions on the order of 10 cm and is referred to as a tile. Each tile is a multi-layer and multi-functional flexible sandwich structure that integrates photovoltaics, DC-RF converters, and microwave radiators capable of collecting incident solar power and transmitting it to a receiving station [5, 44].

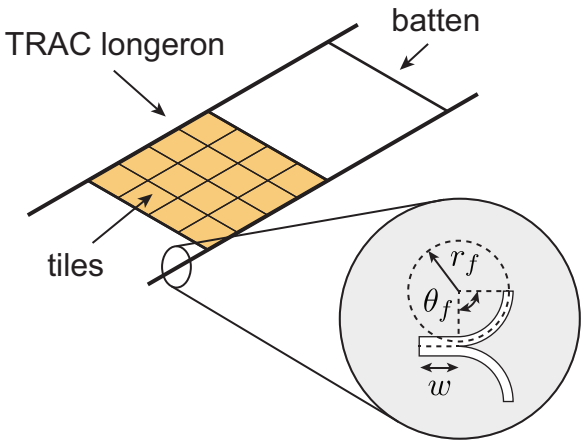

Fig. 7 Strip architecture and cross-sectional geometry of a TRAC longeron parameterized by the web width w flange radius r_f, and flange opening angle θ_f.

The tiles are mounted to slender thin-ply composite structures called strips [45]. Strips are ultralight, ladder-like structures assembled from two longerons connected by 1-m-long transverse battens spaced 1 m apart; see Fig. 7. Each longeron is a triangular rollable and collapsible (TRAC) boom [46] with the nominal material and geometric properties (12.7-mm flange radius, 8-mm web width, and 90-deg flange opening angle) from the numerical model used in a recent study of strip deployment dynamics [47], which in turn is based on a recent experimental characterization of the TRAC longerons [48]. These longerons trace their heritage back to the original Caltech SSPP design study [6] and are sized for

the expected solar radiation pressure load on a 60 m × 60 m spacecraft. The longerons contribute bending and shear stiffnesses to the strip. Each batten is a pultruded carbon fiber rod modeled as an isotropic beam with a rectangular cross-section of breadth 3 mm (in the plane of the strip) and height 0.6 mm with the material properties from [47]. The battens contribute lateral bending stiffness and support the tiles. The strips are stiff in torsion due to the combination of longerons and battens. Strips have a uniform areal mass density of 100 g/m^2 to account for both the tiles and the underlying structure. To increase the computational tractability of the numerical model, rectangular strips modeled as elastic beams replace the thin-shell trapezoidal strips described in the original SSPP concept.

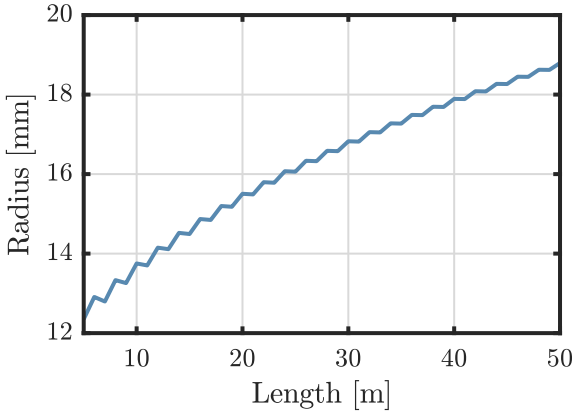

Fig. 8 Boom radii as a function of spacecraft size.

Each strip is attached to two diagonal booms. The booms are modeled as isotropic thin-walled cylindrical tubes with the material properties from [15] (density 1600 kg/m^3, elastic modulus 70 GPa, and Poisson's ratio 0.3) and a wall thickness-to-radius ratio of 0.03. The thin-walled circular cross-section and isotropic material properties are intended to approximate the expected stiffness properties of the deployable, closed cross-section composite booms likely to be used on an actual spacecraft. For mass-efficiency, the booms must not be overly stiff. However, since the inertial loads induced by slew maneuvers increase as spacecraft size increases, there is a general requirement for stiffer booms on larger spacecraft. The optimal boom size depends on the loading, spacecraft size, structural limits (e.g., due to buckling), and deflection limits [15], i.e., the proportion of the deflection in the strips versus the booms. In this case, the boom radii are taken from the design study in Chapter 7 of [8] and sized to carry 40% of the maximum deflection under the expected slew maneuver loads. The design study assumes that the inertial loads are the critical load case, as opposed to, e.g., environmental loads like solar radiation pressure. This is generally the case for fast slew maneuvers of large, plate-like spacecraft [8]. With the 40% deflection constraint, the maximum boom and strip deflections are approximately equal, leading to mass-efficient boom designs. Figure 8 plots the boom radii as a function of the spacecraft size. These radii correspond to linear mass densities between 0.04 kg m^{-1} and 0.12 kg m^{-1}. The boom radii, linear mass densities, and resulting bending stiffnesses are comparable to those from other large flexible spacecraft concepts; see e.g., [49, 50]. Note that the "scalloping" in the figures is an artifact of the modeling assumptions. Specifically, larger gaps between the strips for spacecraft with odd integer side lengths have the effect of decreasing the spacecraft's average areal density, which in turn decreases the slew maneuver loads on the structure.

The four booms are arranged with angular spacings of 90 deg and cantilevered to a central hub. The areas between two adjacent booms define identical quadrants, each containing n rectangular strips of width b (in this case, $b = 1$ m) uniformly spaced a distance d apart; see Fig. 9. The length ℓ_n of the outermost strip and b determine the geometry of the quadrant. Specifically, the number of strips is

$$n = \left\lfloor \frac{(\ell_n/2)}{b} \right\rfloor \tag{57}$$

where $\lfloor \cdot \rfloor$ denotes rounding down to the nearest integer. Equation (57) assumes that the distance from the central hub to the edge of the innermost strip is $b/2$ (resulting in an innermost strip of length $\ell_1 = 2b$) and that the outermost strip attaches to the ends of the booms. This leaves a square hole with sides of length b at the center of the spacecraft for the

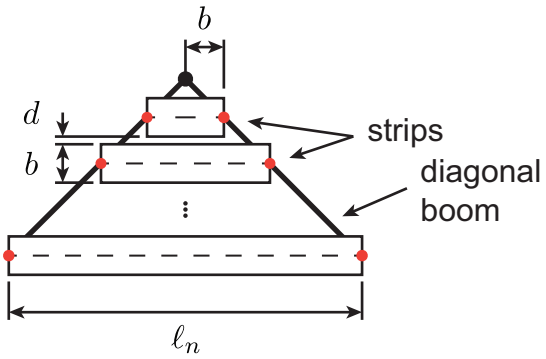

Fig. 9 Geometry of a quadrant of a complete SSPP-like spacecraft. The corners of each rectangular strip overlap the strips in adjacent quadrants.

central hub. The spacing d between the strips and the length ℓ_i of the ith strip then follow as

$$d = (\ell_n/2 - nb)\,/(n-1) \tag{58}$$

$$\ell_i = 2\,(ib + (i-1)d) \tag{59}$$

where $i = 1$ and $i = n$ denote the innermost and outermost strips, respectively. In the numerical model, each strip is idealized as a beam with its axis coincident with its centerline; Fig. 9 denotes each centerline by a dashed line. Additionally, the sequel only considers spacecraft with integer-length outermost strips. If the length ℓ_n of the outermost strip is even, there are $n = \ell_n/2$ strips per quadrant and no spaces between adjacent strips. However, if ℓ_n is odd, then there are $n = (\ell_n - 1)/2$ strips per quadrant, leading to spaces between adjacent strips.

The combination of the tiles, strips, booms, and central hub constitute the spacecraft. The central hub includes the deployment mechanism and spacecraft bus, the latter of which provides the requisite spacecraft functions like attitude determination and control, command and data handling, propulsion, and communications. The deployment mechanism is modeled as a lumped mass of 40 kg. This estimate is based on scaling the measured mass plus contingencies of the engineering model of the deployment mechanism for the DOLCE technology demonstration mission [51] to accommodate 1-m-wide strips and accounting for future mass optimization. The spacecraft bus is then modeled as a lumped mass of 80 kg. This estimate is based on state-of-the-art small satellite technology, although in reality the bus mass may vary widely depending on the requirements of a given mission. The bus moments of inertia are neglected because they are expected to be small relative to the moments of inertia of the deployed structure.

The spacecraft is modeled as a flexible multibody system using the geometrically nonlinear Timoshenko beam finite elements from [8] to discretize the booms and strips. These elements are a structure-preserving, quaternion-based reformulation of the geometrically exact beam finite elements introduced in [52]. The translational and rotational inertia forces in the finite element model are respectively integrated using full integration and 5-point Gaussian quadrature. To alleviate shear locking, the internal elastic forces are then integrated using 1-point reduced integration and MacNeal's residual bending flexibility correction [53]. With 1-point reduced integration, the internal forces and moments in each element are constant, leading to force and moment discontinuities between elements. Mesh convergence requires a reasonably smooth variation in the internal forces and moments across the structure. The results of a mesh convergence study indicate that convergence occurs with maximum element lengths on the order of 1 m, irrespective of the size of the structure. For this reason, the finite element mesh uses elements with maximum lengths of 1 m.

To simplify the structural architecture, the model eliminates the diagonal cords used to support the strips in [6], instead attaching each strip directly to the corresponding diagonal booms using revolute joints with rotation axes parallel to the booms. For this reason, the spacecraft studied here are referred to as *SSPP-like*. Mathematically, the flexible multibody dynamics model is a system of nonlinear differential algebraic equations with holonomic constraints enforced via the method of Lagrange multipliers [24]. In what follows, the flexible multibody dynamics model is sometimes referred to as the full finite element model.

Since the strips are slender, thin-shell structures, modeling them as beams requires evaluating their equivalent beam cross-sectional properties. This is done by applying an energy-equivalence-based homogenization procedure to high-fidelity strip finite element models; for additional details, see [8]. The equivalent beam properties are inputs to the

flexible multibody dynamics model. Replacing the strips with beams limits the model to the simulation of macroscale structural dynamics.

For the modal analysis and the subsequent model reduction, the flexible multibody dynamics model is linearized at rest in its undeformed configuration with the 6 DOFs at the central hub node fully restrained. A Galerkin projection onto the null space of the constraint gradient matrix is then used to convert the linearized equations of motion to a standard form for modal analysis.

B. Minimum Slew Times Predictions

Minimum slew times were evaluated for SSPP-like spacecraft with integer edge lengths from 5 m to 50 m. These spacecraft have first-mode natural frequencies between 1 Hz and 1 mHz.

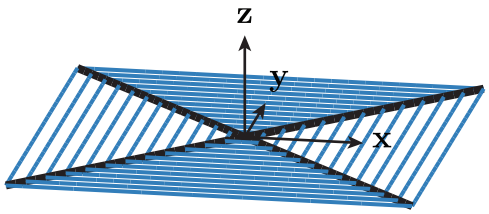

Fig. 10 Rotation axes for y-axis slew maneuver.

Due to its improved performance relative to a bang-bang slew, subsequent developments only consider a 90-deg, single-axis polynomial slew maneuver (Fig. 3) about the **y**-axis from Fig. 10. The maneuver rotates the spacecraft about the **y**-axis from an initial orientation of 0 deg to a final one of 90 deg in time T.

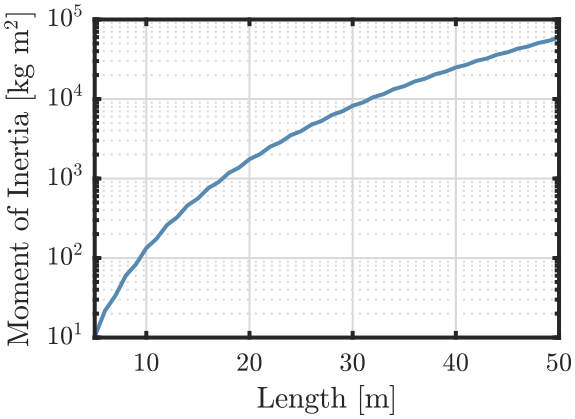

Fig. 11 Moment of inertia J_{yy} about y-axis as a function of edge length.

Following Sec. IV.C, the feasible slew time calculations are based on undamped canonical flexible spacecraft models (Fig. 2) derived from the corresponding full finite element models. Each canonical model requires three inputs: the rigid body moment of inertia about the slew axis (in this case, J_{yy}), the dominant-mode frequency, and the corresponding modal inertia. For each edge length, J_{yy} is calculated directly from the mass matrix of the corresponding full finite element model. Figure 11 depicts the resulting J_{yy} as a function of edge length.

The dominant-mode frequency and modal inertia are determined from a modal analysis of the corresponding full finite element model. For a single axis slew, the dominant mode is the mode with the highest modal inertia about the slew axis. The modal inertia is the main diagonal entry corresponding to the slew axis in the modal mass matrix $\mathbf{M}_i$ from Sec. III. Figure 12 compares the first-mode and dominant-mode frequencies as a function of the spacecraft size. The figure emphasizes that the first mode is not the dominant mode for a single-axis slew; instead, the dominant mode is either mode 2 or mode 3. Note that the 24 m $\times$ 24 m spacecraft has first-mode and dominant-mode frequencies of approximately 25 mHz and 28 mHz, respectively.

Modes 2 and 3 are symmetric, meaning that they share the same natural frequency and that mode 3 is the same as

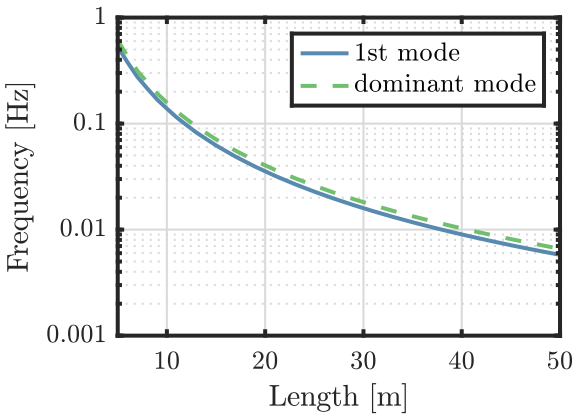

Fig. 12 Comparison of first-mode and dominant-mode natural frequencies. The dominant mode for a slew maneuver is the mode with the highest modal inertia about the slew axis.

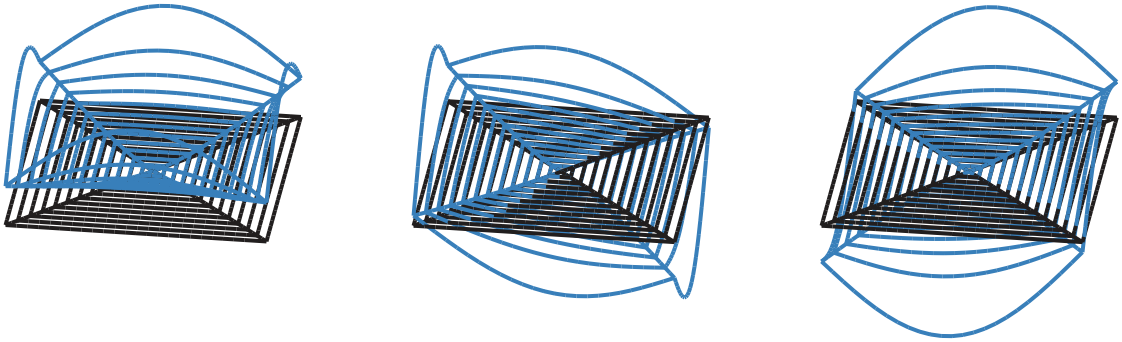

(a) **(b)** **(c)**

Fig. 13 (a) first mode, (b) dominant mode, and (c) symmetric mode at dominant-mode frequency for a 24 m × 24 m SSPP-like spacecraft.

mode 2 after a symmetry transformation, as shown in Fig. 13 for the 24 m × 24 m SSPP-like spacecraft. The modes in Fig. 13 are representative of the first three modes for the range of considered edge lengths. The first mode (Fig. 13a) excites symmetric bending deflections across all four quadrants. In contrast, modes 2 and 3 excite antisymmetric bending deflections; mode 2 is identical to mode 3 after a 90 deg counterclockwise rotation about the spacecraft's out-of-plane axis. Since modes 2 and 3 are symmetric, each reduced-order model must include the total modal inertia in both modes 2 and 3. Due to symmetry, these models have two degrees of freedom but include three modes: a rigid body mode and two symmetric flexible modes.

The reduced-order models are used to predict slew times for SSPP-like flexible spacecraft with integer edge lengths from 5 m to 50 m. The slew time calculations require two additional inputs: a slew maneuver and a slew performance metric. In this case, the slew maneuver is the 90-deg polynomial slew from Fig. 3 and the slew performance metric is a requirement on the maximum amplitude of the residual angular velocity (see Sec. IV). The amplitude of the residual angular velocity is a measure of the residual flexible dynamics after the completion of the slew. Two requirements on the residual angular velocity are considered, 0.01 deg/sec and 0.001 deg/sec, which respectively correspond to relatively coarse and fine pointing requirements. The minimum slew time corresponds to the fastest slew that guarantees that the residual angular velocity is always less than or equal to the specified requirement. In what follows, the resulting slew times are referred to as the structure-based slew performance limits.

The structure-based slew performance limits are also compared to slew performance limits associated with the available angular momentum and torque of reaction wheels for representative attitude control systems. Two reaction

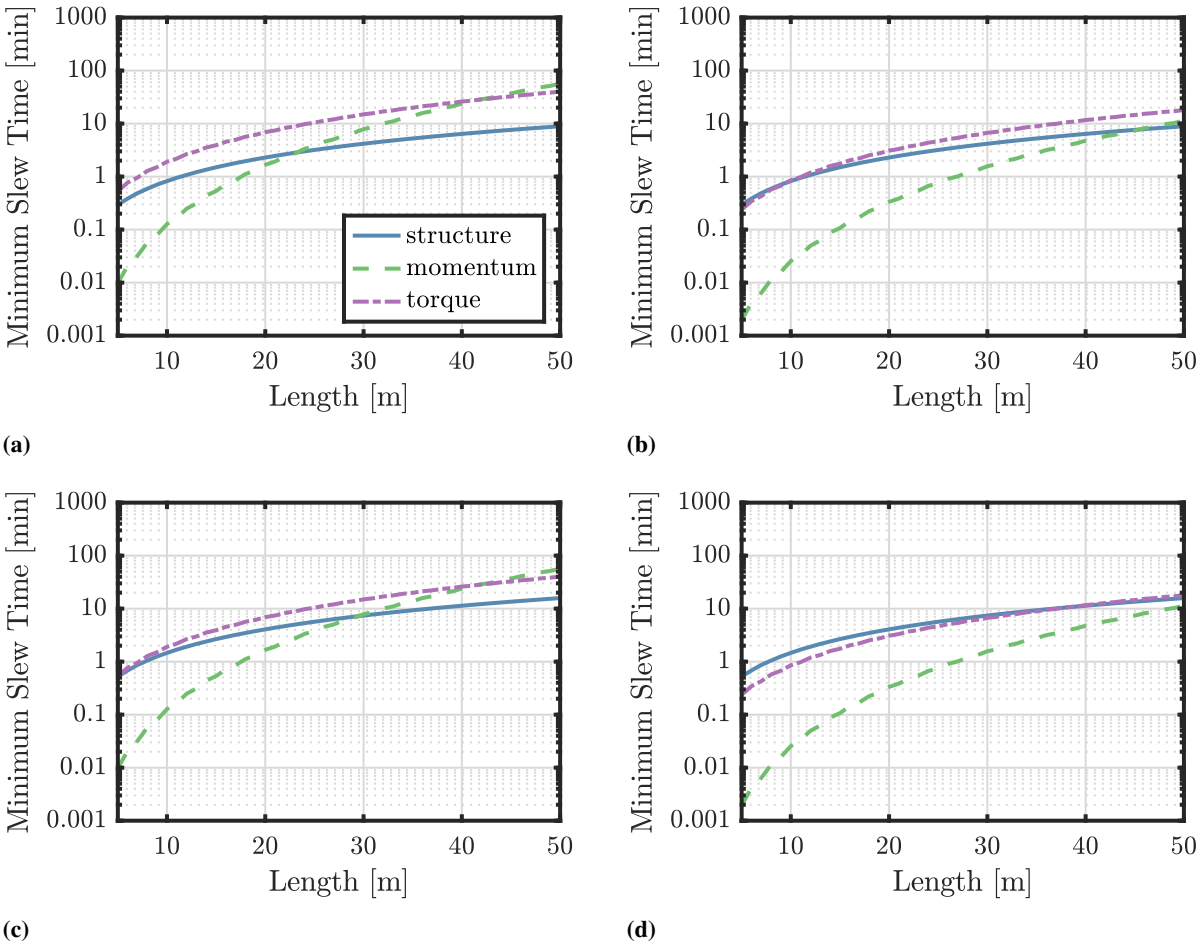

Fig. 14 Comparison of minimum slew times for polynomial slew maneuver. (a) baseline reaction wheel, 0.01 deg/sec; (b) 5× baseline reaction wheel, 0.01 deg/sec; (c) baseline reaction wheel, 0.001 deg/sec; (d) 5× baseline reaction wheel, 0.001 deg/sec.

wheels are considered. The first is a baseline wheel with a maximum torque of 0.2 N m and 100 N m s of angular momentum storage. This is representative of large, commercially available reaction wheels. The second is a reaction wheel with five times the maximum torque and momentum of the baseline wheel. Additionally, it is assumed that only 60% of the total momentum and torque are available for slews. Momentum and torque are allocated with margins for different ACS functions, including feedforward control (slews), feedback control, and to account for wheel friction and gyroscopic effects. As a result, only a fraction of the total momentum and torque are ever available for slews. For example, the Cassini spacecraft allocated 12.5% of its total torque for slews [54]; more agile spacecraft require higher momentum and torque allocations for slews. However, 60% is likely overly generous because increasing the available angular momentum for a slew requires increasing the depth of desaturation before the slew. The momentum and torque limits constrain the maximum angular velocity and acceleration, which in turn constrain the minimum slew time.

Figure 14 depicts the minimum slew times as a function of the spacecraft size. In each sub-figure, the top-most curve is the most-restrictive constraint on slew performance, and hence, determines the minimum slew time. With the baseline reaction wheel, Figs. 14a and 14c demonstrate that the slew performance limit is due to either the available torque or momentum, not the structure, regardless of the requirement on the residual angular velocity. Similarly, with the larger reaction wheel and the coarser pointing requirement, Fig. 14b shows that the available torque again typically drives the minimum slew time. The only exception is the case with the larger reaction wheels and the finer pointing requirement; see Fig. 14d. In this case, the structure-based performance limit constrains the minimum slew time for spacecraft at length scales below approximately 40 m. Above 40 m, the slew times are again torque-constrained. Even so, below the crossover point, the structure-based and torque-based performance limits result in comparable minimum slew times.

Decreasing (i) the fraction of the momentum and torque available for slews, (ii) the maximum momentum and torque, or (iii) the requirement on the amplitude of the residual angular velocity shifts the corresponding curves in Fig. 14 up.

Based on Fig. 14, the capabilities of each spacecraft's ACS are often significantly more limiting than the dynamics of the structure. When this is the case, the results suggest that a lighter-weight, less-stiff, and potentially lower-cost structure can be used to shift the structure-based performance limit closer to those of the ACS, at least as far as slewing is concerned. The figure likewise emphasizes that SSPP-like flexible spacecraft can likely achieve slew times on the order of 10 min or less for 90-deg, single-axis maneuvers, even at length scales as large as 50 m.

This analysis also demonstrates that common heuristics for designing flexible spacecraft slew maneuvers may be overly conservative. For example, for the 24 m × 24 m spacecraft, the structure-based slew times in Fig. 14 for the coarse and fine pointing requirements correspond to constraints of $T/T_n \geq 5.1$ and $T/T_n \geq 9.0$, respectively (relative to the first-mode period, these constraints are $T/T_1 \geq 4.5$ and $T/T_1 \geq 7.9$). On the other hand, a heuristic-based constraint may instead require that $T/T_n \geq 10$. Altogether, this further emphasizes how the minimum T/T_n (or T/T_1) depends on the pointing requirements, the spacecraft, and the slew maneuver.

To verify these results, the next section compares the predictions from the reduced-order model for the 24 m × 24 m spacecraft with those from geometrically nonlinear simulations of the corresponding full finite element model.

C. Slew Time Verification

Time-domain simulations of the 24 m × 24 m SSPP-like spacecraft were used to verify the slew time predictions from Sec. V.B. The simulations considered 90-deg, single-axis polynomial slew maneuvers about the **y**-axis from Fig. 10 with durations from 1 min to 20 min. A 1-min slew duration is comparable to the spacecraft's fundamental period of 40.4 s, i.e., $T/T_1 \approx 1$; see Fig. 12.

The dynamic simulations integrated the full finite element model using a quaternion-based implementation of the Lie group generalized-α method [55, 56] with a time step size of 0.01 s. Larger time steps lead to numerical instabilities for faster slew maneuvers. The solver uses an infinity-norm-based convergence criterion with an absolute convergence tolerance of 10^{-6} for both the generalized force and constraint residuals and uses the optimal scaling strategy from [57] to avoid numerical ill-conditioning; for additional details regarding the solver implementation, see [8].

The Lie group generalized-α method includes numerical dissipation specified by the spectral radius at infinity $\rho_\infty \in [0, 1]$ [58]. For flexible multibody systems, this numerical dissipation eliminates the high-frequency numerical oscillations associated with the solution of numerically stiff differential equations and stabilizes the weak numerical instability attributed to the constraints [59]. Here, the simulations use $\rho_\infty = 0.7$. This results in a low-to-moderate amount of high-frequency numerical dissipation. However, physically accurate simulations often require both physical damping to attenuate low frequencies and numerical damping to attenuate higher ones [60]. For this reason, viscoelastic Kelvin-Voigt damping [61] is incorporated into the finite element model to replicate the very low modal damping characteristic of large space structures [41]. The Kelvin-Voigt damping coefficients were calculated using the optimization-based approach from [8] such that the tangent damping matrix in the spacecraft's undeformed configuration corresponds to stiffness-proportional damping with 0.25% of critical damping in the first mode.

The simulations were divided into three steps:

1) for $t < 0$, spacecraft at rest in its undeformed configuration;
2) for $0 \leq t < T$, spacecraft actuated by a body-fixed external moment $M_y(t) = J_{yy}\ddot{\theta}(t)$ applied at its central node where $\ddot{\theta}(t)$ is the angular acceleration for the polynomial slew maneuver from Fig. 3; and
3) for $t \geq T$, spacecraft unactuated and undergoing damped free vibrations (the residual flexible dynamics).

The simulations terminate at some time $t_f > T$ to study the residual flexible dynamics.

Verifying the slew time calculations from Sec. V involves comparing the amplitudes of the residual angular velocities predicted by the reduced-order model from Sec. V.B with the predictions from the full finite element model as functions of slew time. For the full finite element model, the amplitude of the residual spacecraft bus angular velocity, denoted Ω, was calculated from

$$\mathrm{KE}(T) + \mathrm{SE}(T) = \frac{1}{2} J_{yy} \Omega^2 \tag{60}$$

where KE and SE are the kinetic and strain energies. Thus, Ω is the angular velocity that results from converting the spacecraft's residual strain energy into kinetic energy about the slew axis.

Figure 15 compares the results. Based on Fig. 15, the predictions from the reduced-order model show good agreement with the full finite element model. This indicates that the two symmetric flexible modes in the reduced-order model are important contributors to the dynamic response and suggests that the elastic deformations remain in the small-deflection regime despite the large rigid body rotation during the slew maneuver. However, some caution is

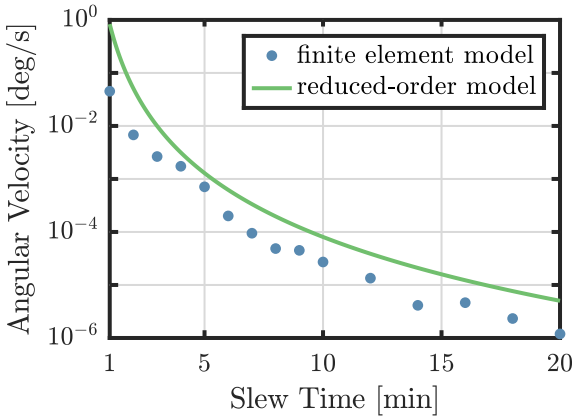

Fig. 15 Amplitude of the residual spacecraft bus angular velocity as a function of slew time.

warranted here. Even though the reduced-order model accurately predicts the residual angular velocity, this by no means guarantees that the reduced-order model also accurately predicts other figures of merit, e.g., the internal forces and moments in the structure. Moreover, since the reduced-order model consistently overestimates Ω, the results demonstrate that its predictions are both accurate and conservative, at least for the 24 m $\times$ 24 m spacecraft. Taken together, Figs. 14 and 15 imply that it is feasible to slew a 24 m $\times$ 24 m flexible spacecraft with a first-mode frequency of approximately 25 mHz 90 deg about a single-axis in 10 min or less. This is significantly faster than the current state-of-practice.

VI. Conclusion

This paper has studied the slew maneuver performance of agile flexible spacecraft. Given a spacecraft and slew maneuver, the paper proposes using reduced-order modal models and a requirement on the magnitude of the disturbance due to the residual flexible dynamics from a slew to determine constraints on the minimum feasible slew time.

The analysis has highlighted that both the shape of the slew maneuver and the ratio T/T_n between the slew time T and fundamental natural period T_n determine the magnitude of the disturbance due to the residual flexible dynamics. To explain this result, it was shown that that even a simple smooth slew maneuver significantly reduces the residual flexible dynamics, in this case, by several orders of magnitude relative to a baseline "bang-bang" slew. This suggests that there is an opportunity to use modern robust optimal control [62–64] to design slew maneuvers that are simultaneously robust to the uncertainties inherent to flexible spacecraft structures (something driven, at least in part, by the inability to test them in representative 0-g environments before launch), minimize the residual flexible dynamics, and satisfy any other constraints on the system. Perhaps most importantly, these maneuvers can likely be flown using existing attitude control systems, making them a potentially low-risk approach for improving the performance of flexible spacecraft.

As a case study, the paper has predicted the slew performance of a representative very flexible spacecraft based on the Caltech Space Solar Power Project structural architecture [6]. These results have demonstrated that a large flexible spacecraft with a 25-mHz first-mode frequency can be slewed 90 deg in 10 min or less, at least as far as the structure is concerned. This is at least one to two orders of magnitude faster than the current state-of-practice.

These results demonstrate that, contrary to common assumptions, structure-based slew performance limits are often less-restrictive than those associated with other constraints on the system. In particular, they show that an attitude control system's available angular momentum and torque are often significantly more limiting than the structure. For these reasons, existing spacecraft designs are likely overly stiff with overly conservative design margins, which suggests that there are opportunities to either maneuver flexible spacecraft faster (provided sufficiently capable actuators are available) or fly less-conservative, lighter-weight, and potentially lower-cost spacecraft structures. However, efforts to fly such structures must acknowledge that slewing is just one of many important structural design drivers. For example, the constraints associated with other structural design drivers, like launch loads and propulsive maneuvers, may ultimately limit the achievable performance gains.

Funding Sources

M. A. Marshall was supported by a NASA Space Technology Research Fellowship. Financial support from the California Institute of Technology (Caltech) Space Solar Power Project is also gratefully acknowledged.

Acknowledgments

The authors thank Antonio Pedivellano for help in developing the high-fidelity Abaqus finite element model used in the homogenization procedure mentioned in Sec. V. The authors likewise thank Dan Scharf, W. Keats Wilkie, and Jay Warren for the helpful comments and insightful discussions regarding this work. This work benefited from ideas and discussions with Mike Paul Hughes and the other participants at the "Non-Nuclear Exploration of the Solar System" workshop organized by the W. M. Keck Institute for Space Studies in April 2021.

References

[1] Arya, M., Mechentel, F. S., Webb, D. R., Steeves, J. B., Lisman, D., Shaklan, S. B., Bradford, S. C., Kelso, E., Neff, K., Swain, A., Iskra, A., Beidleman, N., Stienmier, J. D., Freebury, G., Tomchek, A., Thomas, T., Hazelton, C., Butler, K., Medina, K., Pulford, M., Adams, L., Hepper, D., and Turse, D., "Demonstration of deployment repeatability of key subsystems of a furled starshade architecture," *Journal of Astronomical Telescopes, Instruments, and Systems*, Vol. 7, No. 2, 2021, p. 021202. doi:10.1117/1.JATIS.7.2.021202.

[2] Brophy, J., Pellegrino, S., Lubin, P., Alkalai, L., Atwater, H., Biswas, A., Boca, A., Carr, G., Davoyan, A., Frazier, W., Gdoutos, T., Grandidier, J., Hogstrom, K., Hughes, M., Johnson, L., Kelzenberg, M., Lee, A., Luther, J., Marshall, M., Marrese-Reading, C., McCarty, S., McNutt, R., Petro, E., Polk, J., Scully, J., Sekerak, M., and Sellers, I., "Non-Nuclear Exploration of the Solar System Study," Tech. rep., W. M. Keck Institute for Space Studies, Pasadena, California, 2022. doi:10.7907/h62p-6328.

[3] Lockett, T. R., Castillo-Rogez, J., Johnson, L., Matus, J., Lightholder, J., Marinan, A., and Few, A., "Near-Earth Asteroid Scout flight mission," *IEEE Aerospace and Electronic Systems Magazine*, Vol. 35, No. 3, 2020, pp. 20–29. doi:10.1109/MAES.2019.2958729.

[4] Kobayashi, K., Johnson, L., Thomas, H. D., McIntosh, S., McKenzie, D., Newmark, J., Heaton, A., Carr, J., Baysinger, M., Bean, Q., Fabisinski, L., Capizzo, P., Clements, K., Sutherlin, S., Garcia, J., Medina, K., and Turse, D., "The high inclination solar mission," `https://arxiv.org/abs/2006.03111`, arXiv:2006.03111. Accessed June 4, 2021, 2020.

[5] Hashemi, M. R. M., Fikes, A. C., Gal-Katziri, M., Abiri, B., Bohn, F., Safaripour, A., Kelzenberg, M. D., Warmann, E. L., Espinet, P., Vaidya, N., Gdoutos, E. E., Leclerc, C., Royer, F., Pellegrino, S., Atwater, H. A., and Hajimiri, A., "A flexible phased array system with low areal mass density," *Nature Electronics*, Vol. 2, 2019, pp. 195–205. doi:10.1038/s41928-019-0247-9.

[6] Arya, M., Lee, N., and Pellegrino, S., "Ultralight structures for space solar power satellites," *AIAA SciTech Forum*, San Diego, California, 2016. doi:10.2514/6.2016-1950, AIAA 2016-1950.

[7] Marshall, M. A., Goel, A., and Pellegrino, S., "Power-optimal guidance for planar space solar power satellites," *Journal of Guidance, Control, and Dynamics*, Vol. 43, No. 3, 2020, pp. 518–535. doi:10.2514/1.G004643.

[8] Marshall, M. A., "Dynamics of Ultralight Flexible Spacecraft during Slew Maneuvers," Ph.D. thesis, California Institute of Technology, Pasadena, California, 2022. doi:10.7907/w6na-w476.

[9] Vu-Quoc, L., and Simo, J. C., "Dynamics of Earth-orbiting flexible satellites with multibody components," *Journal of Guidance, Control, and Dynamics*, Vol. 10, No. 6, 1987, pp. 549–558. doi:10.2514/3.20255.

[10] Li, Q., Deng, Z., Zhang, K., and Huang, H., "Unified modeling method for large space structures using absolute nodal coordinate," *AIAA Journal*, Vol. 56, No. 10, 2018, pp. 4146–4157. doi:10.2514/1.J057117.

[11] Sakamoto, H., Miyazaki, Y., and Park, K. C., "Finite element modeling of sail deformation under solar radiation pressure," *Journal of Spacecraft and Rockets*, Vol. 44, No. 3, 2007, pp. 514–521. doi:10.2514/1.23474.

[12] Choi, M., and Damaren, C. J., "Structural dynamics and attitude control of a solar sail using tip vanes," *Journal of Spacecraft and Rockets*, Vol. 52, No. 6, 2015, pp. 1665–1679. doi:10.2514/1.A33179.

[13] Wilkie, W. K., Warren, J., Horta, L. G., Lyle, K. H., Juang, J.-N., Gibbs, S. C., Dowell, E., Guerrant, D. V., and Lawrence, D. A., "Recent advances in heliogyro solar sail structural dynamics, stability, and control research," *AIAA SciTech Forum*, Kissimmee, Florida, 2015. doi:10.2514/6.2015-0431, AIAA 2015-0431.

[14] Arya, M., Hodges, R., Sauder, J. F., Horst, S., Mobrem, M., Pedivellano, A., Wen, A., Truong, A., and Pellegrino, S., "Lightweight composite reflectarray that can be flattened, folded, and coiled for compact stowage," *AIAA SciTech Forum*, San Diego, California, 2022. doi:10.2514/6.2022-1886, AIAA 2022-1886.

[15] Lee, A. J., and Pellegrino, S., "Mass efficiency of strip-based coilable space structures," *International Journal of Solids and Structures*, Vol. 254–255, 2022, p. 111867. doi:10.1016/j.ijsolstr.2022.111867.

[16] Craig Jr., R. R., and Bampton, M. C. C., "Coupling of substructures for dynamic analyses," *AIAA Journal*, Vol. 6, No. 7, 1968, pp. 1313–1319. doi:10.2514/3.4741.

[17] Spanos., J. T., "Control-structure interaction in precision pointing servo loops," *Journal of Guidance, Control, and Dynamics*, Vol. 12, No. 2, 1989, pp. 256–263. doi:10.2514/3.20399.

[18] Wie, B., *Space Vehicle Dynamics and Control*, 2nd ed., American Institute of Aeronautics and Astronautics, Reston, Virginia, 2008. doi:10.2514/4.860119.

[19] Sutter, T. R., Cooper, P. A., Young, J. W., and McCutchen, D. K., "Dynamic and attitude control characteristics of an International Space Station," *28th Structures, Structural Dynamics and Materials Conference*, Monterey, California, 1987. doi:10.2514/6.1987-931, AIAA 87-0931.

[20] Lee, A. Y., Yu, J. W., Kahn, P. B., and Stoller, R. L., "Space interferometry mission spacecraft pointing error budgets," *IEEE Transactions on Aerospace and Electronic Systems*, Vol. 38, No. 2, 2002, pp. 502–514. doi:10.1109/TAES.2002.1008982.

[21] Bayard, D. S., "Spacecraft pointing control criteria for high resolution spectroscopy," *IEEE Transactions on Aerospace and Electronic Systems*, Vol. 35, No. 2, 1999, pp. 637–644. doi:10.1109/7.766944.

[22] Pittelkau, M. E., and McKinley, W. G., "Optical transfer functions, weighting functions, and metrics for images with two-dimensional line-of-sight motion," *Optical Engineering*, Vol. 55, No. 6, 2016, p. 063108. doi:10.1117/1.OE.55.6.063108.

[23] Hedgepeth, J. M., "Critical requirements for the design of large space structures," *2nd AIAA Conference on Large Space Platforms: Toward Permanent Manned Occupancy in Space*, San Diego, California, 1981. doi:10.2514/6.1981-443, AIAA-81-0443.

[24] Géradin, M., and Cardona, A., *Flexible Multibody Dynamics: A Finite Element Approach*, 1st ed., John Wiley & Sons, Chichester, United Kingdom, 2001.

[25] Hager, W. W., "Updating the inverse of a matrix," *SIAM Review*, Vol. 31, No. 2, 1989, pp. 221–239. doi:10.1137/1031049.

[26] Miller, K. S., "On the inverse of the sum of matrices," *Mathematics Magazine*, Vol. 54, No. 2, 1981, pp. 67–72. doi:10.2307/2690437.

[27] Kammer, D. C., and Triller, M. J., "Ranking the dynamic importance of fixed interface modes using a generalization of effective mass," *International Journal of Analytical and Experimental Modal Analysis*, Vol. 9, No. 2, 1994, pp. 77–98.

[28] Triller, M. J., and Kammer, D. C., "Controllability and observability measures for Craig-Bampton substructure representations," *Journal of Guidance, Control, and Dynamics*, Vol. 17, No. 6, 1994, pp. 1198–1204. doi:10.2514/3.21333.

[29] Kammer, D. C., and Triller, M. J., "Selection of component modes for Craig-Bampton substructure representations," *Journal of Vibration and Acoustics*, Vol. 118, No. 2, 1996, pp. 264–270. doi:10.1115/1.2889657.

[30] Moore, B. C., "Principal component analysis in linear systems: Controllability, observability, and model reduction," *IEEE Transactions on Automatic Control*, Vol. 26, No. 1, 1981, pp. 17–32. doi:10.1109/TAC.1981.1102568.

[31] Jonckheere, E. A., "Principal component analysis of flexible systems–Open-loop case," *IEEE Transactions on Automatic Control*, Vol. 29, No. 12, 1984, pp. 1095–1097. doi:10.1109/TAC.1984.1103457.

[32] Zingoni, A., "Group-theoretic exploitations of symmetry in computational solid and structural mechanics," *International Journal for Numerical Methods in Engineering*, Vol. 79, No. 3, 2009, pp. 253–289. doi:10.1002/nme.2576.

[33] McInnes, C. R., "Satellite attitude slew manoeuvres using inverse control," *The Aeronautical Journal*, Vol. 102, No. 1015, 1998, pp. 259–266. doi:10.1017/S0001924000065295.

[34] Hindle, T. A., and Singh, T., "Robust minimum power/jerk control of maneuvering structures," *Journal of Guidance, Control, and Dynamics*, Vol. 24, No. 4, 2001, pp. 816–826. doi:10.2514/2.4783.

[35] Kim, J.-J., and Agrawal, B., "Experiments on jerk-limited slew maneuvers of a flexible spacecraft," *AIAA Guidance, Navigation, and Control Conference*, Keystone, Colorado, 2006. doi:10.2514/6.2006-6187, AIAA 2006-6187.

[36] Leve, F. A., Hamilton, B. J., and Peck, M. A., *Requirements Development for Momentum Control Systems*, 1st ed., Springer, Cham, Switzerland, 2015, Chap. 3, pp. 35–55. doi:10.1007/978-3-319-22563-0_3.

[37] Banerjee, A. K., Pedreiro, N., and Singhose, W. E., "Vibration reduction for flexible spacecraft following momentum dumping with/without slewing," *Journal of Guidance, Control, and Dynamics*, Vol. 24, No. 3, 2001, pp. 417–427. doi:10.2514/2.4737.

[38] Singh, T., and Singhose, W., "Tutorial on input shaping/time delay control of maneuvering flexible structures," *Proceedings of the 2002 American Control Conference*, Vol. 3, Anchorage, Alaska, 2002, pp. 1717–1731. doi:10.1109/ACC.2002.1023813.

[39] Longuski, J. M., Guzmán, J. J., and Prussing, J. E., *Bounded Control Problems*, 1st ed., Springer, New York, 2013, Chap. 9, pp. 175–191. doi:10.1007/978-1-4614-8945-0_9.

[40] Ogata, K., *System Dynamics*, 4th ed., Pearson Education, Inc., Upper Saddle River, New Jersey, 2004, Chap. 10, pp. 513–520.

[41] Balas, M., "Trends in large space structure control theory: Fondest hopes, wildest dreams," *IEEE Transactions on Automatic Control*, Vol. 27, No. 3, 1982, pp. 522–535. doi:10.1109/TAC.1982.1102953.

[42] Orphee, J., Diedrich, B., Stiltner, B. C., and Heaton, A., "Solar torque management for the Near Earth Asteroid Scout CubeSat using center of mass position control," *AIAA SciTech Forum*, Kissimmee, Florida, 2018. doi:10.2514/6.2018-1326, AIAA 2018-1326.

[43] Clough, R. W., and Penzien, J., *Dynamics of Structures*, 1st ed., McGraw-Hill, Inc., New York, 1975, Chap. 6, p. 87.

[44] Gdoutos, E. E., Leclerc, C., Royer, F., Kelzenberg, M. D., Warmann, E. C., Espinet-Gonzalez, P., Vaidya, N., Bohn, F., Abiri, B., Hashemi, M. R., Gal-Katziri, M., Fikes, A., Atwater, H., Hajimiri, A., and Pellegrino, S., "A lightweight tile structure integrating photovoltaic conversion and RF power transfer for space solar power applications," *AIAA SciTech Forum*, Kissimmee, Florida, 2018. doi:10.2514/6.2018-2202, AIAA-2018-2022.

[45] Royer, F., and Pellegrino, S., "Ultralight ladder-type coilable space structures," *AIAA SciTech Forum*, Kissimmee, Florida, 2018. doi:10.2514/6.2018-1200, AIAA 2018-1200.

[46] Murphey, T. W., Turse, D., and Adams, L., "TRAC boom structural mechanics," *AIAA SciTech Forum*, Grapevine, Texas, 2017. doi:10.2514/6.2017-0171, AIAA 2017-0171.

[47] Pedivellano, A., and Pellegrino, S., "Deployment dynamics of thin-shell space structures," *Journal of Spacecraft and Rockets*, Vol. 59, No. 4, 2022, pp. 1214–1227. doi:10.2514/1.A35172.

[48] Leclerc, C., and Pellegrino, S., "Nonlinear elastic buckling of ultra-thin coilable booms," *International Journal of Solids and Structures*, Vol. 203, 2020, pp. 46–56. doi:10.1016/j.ijsolstr.2020.06.042.

[49] Greschik, G., and Mikulas, M. M., "Design study of a square solar sail architecture," *Journal of Spacecraft and Rockets*, Vol. 39, No. 5, 2002, pp. 653–661. doi:10.2514/2.3886.

[50] Murphy, D. M., McEachen, M. E., Macy, B. D., and Gaspar, J. L., "Demonstration of a 20-m solar sail system," *46th AIAA/ASME/ASCE/AHS/ASC Structures, Structural Dynamics and Materials Conference*, Austin, Texas, 2005. doi:10.2514/6.2005-2126, AIAA 2005-2126.

[51] Gdoutos, E. E., Sommer, C. F., Truong, A., Wen, A., Pedivellano, A., Ubamanyu, U. K., Madonna, R. G., and Pellegrino, S., "Development of the Deployable on-Orbit ultraLight Composite Experiment (DOLCE) for the Space Solar Power Project Demonstration Mission," *AIAA SciTech Forum*, San Diego, California, 2022. doi:10.2514/6.2022-1266, AIAA 2022-1266.

[52] Cardona, A., and Géradin, M., "A beam finite element non-linear theory with finite rotations," *International Journal for Numerical Methods in Engineering*, Vol. 26, No. 11, 1988, pp. 2403–2438. doi:10.1002/nme.1620261105.

[53] MacNeal, R. H., "A simple quadrilateral shell element," *Computers & Structures*, Vol. 8, No. 2, 1978, pp. 175–183. doi:10.1016/0045-7949(78)90020-2.

[54] Macala, G. A., "Design of the reaction wheel attitude control system for the Cassini spacecraft," *AAS/AIAA Space Flight Mechanics Meeting*, San Diego, California, 2002. AAS 02-121.

[55] Brüls, O., and Cardona, A., "On the use of Lie group time integrators in multibody dynamics," *Journal of Computational and Nonlinear Dynamics*, Vol. 5, No. 3, 2010, p. 031002. doi:10.1115/1.4001370.

[56] Brüls, O., Cardona, A., and Arnold, M., "Lie group generalized-α time integration of constrained flexible multibody systems," *Mechanism and Machine Theory*, Vol. 48, 2012, pp. 121–137. doi:10.1016/j.mechmachtheory.2011.07.017.

[57] Bottasso, C. L., Dopico, D., and Trainelli, L., "On the optimal scaling of index three DAEs in multibody dynamics," *Multibody System Dynamics*, Vol. 19, 2008, pp. 3–20. doi:10.1007/s11044-007-9051-9.

[58] Chung, J., and Hulbert, G. M., "A time integration algorithm for structural dynamics with improved numerical dissipation: The generalized-α method," *Journal of Applied Mechanics*, Vol. 60, No. 2, 1993, pp. 371–375. doi:10.1115/1.2900803.

[59] Cardona, A., and Géradin, M., "Time integration of the equations of motion in mechanism analysis," *Computers & Structures*, Vol. 33, No. 3, 1989, pp. 801–820. doi:10.1016/0045-7949(89)90255-1.

[60] Dewalque, F., Rochus, P., and Brüls, O., "Importance of structural damping in the dynamic analysis of compliant deployable structures," *Acta Astronautica*, Vol. 111, 2015, pp. 323–333. doi:10.1016/j.actaastro.2015.03.003.

[61] Lang, H., Linn, J., and Arnold, M., "Multi-body dynamics simulation of geometrically exact Cosserat rods," *Multibody System Dynamics*, Vol. 25, 2011, pp. 285–312. doi:10.1007/s11044-010-9223-x.

[62] Ross, I. M., Proulx, R. J., Karpenko, M., and Gong, Q., "Riemann–Stieltjes optimal control problems for uncertain dynamic systems," *Journal of Guidance, Control, and Dynamics*, Vol. 38, No. 7, 2015, pp. 1251–1263. doi:10.2514/1.G000505.

[63] Boutselis, G. I., Pan, Y., and Theodorou, E. A., "Numerical trajectory optimization for stochastic mechanical systems," *SIAM Journal on Scientific Computing*, Vol. 41, No. 4, 2019, pp. A2065–A2087. doi:10.1137/17M116272X.

[64] Manchester, Z., and Kuindersma, S., "Robust direct trajectory optimization using approximate invariant funnels," *Autonomous Robots*, Vol. 43, 2019, pp. 375–387. doi:10.1007/s10514-018-9779-5.